Quantifying water storage change and land subsidence induced by reservoir impoundment using GRACE, Landsat, and GPS data

Natthachet Tangdamrongsub [a,b *], Shin-Chan Han [c], Michael F. Jasinski [b], Michal Šprlák [c]

[a] Earth System Science Interdisciplinary Center, University of Maryland, College Park, Maryland, USA

[b] Hydrological Sciences Laboratory, NASA Goddard Space Flight Center, Greenbelt, Maryland, USA

[c] School of Engineering, Faculty of Engineering and Built Environment, The University of Newcastle, Callaghan, New South Wales, Australia

* Correspondence to: natthachet.tangdamrongsub@nasa.gov

Abstract

The construction of hydropower dams is a common strategy to support a country's increasing need for electricity and river water management for industry and agriculture. Although the hydrological and geophysical impacts of water relocation are usually assessed prior to impoundment, their accuracy is generally limited due to the lack of in situ observations, especially in a remote area. This study presents a workflow to quantify the terrestrial water storage change (ΔTWS) and land subsidence induced by a reservoir's water impoundment using multiple satellite observations (GRACE, Landsat), land surface models (CABLE, GLDAS, NCEP, ECMWF), and GPS data. The study site is the Bakun Dam, located in Sarawak, Malaysia, which is the largest hydropower dam in Southeast Asia. Commencing operation in late 2010, the dam induced a change of water mass and lake surface area that was clearly observed by GRACE and Landsat observations, respectively. During the 17-month impounding period (from August 2010 to December 2011), GRACE observed a dramatic increase of approximately 200 mm equivalent water height, while Landsat detected an increased lake extent of around 600 km^2. In this paper, a forward model is developed to determine the increased water surface

level corresponding to GRACE observations, estimated to be about 120 m. In contrast to GRACE, the TWS derived from land surface models cannot capture the increased ΔTWS, due to the lack of reservoir routing algorithms in the models. In addition, the land subsidence was calculated using the disk load model constructed based on the GRACE-derived lake level and Landsat-derived lake extent; the result is validated with the GPS data from BIN1 station, located at the western coast of Borneo. The commencement stage of the Bakun Dam induces the large-scale land subsidence, which causes the GPS-BIN1 station to subside by ~9 mm, and move toward the Bakun Lake by ~4 mm. Computation of the surface displacements directly from GRACE spherical harmonic coefficient data fails to capture the subsidence feature, mainly due to the truncation error. Overall, this study demonstrates that evaluating GRACE in conjunction with Landsat, LSMs, and GPS data allows the exploitation of the gravity signal at a much smaller spatial scale than its intrinsic resolution. Benefiting from global coverage, the newly developed satellite-based algorithm is a valuable tool for assessing the impacts of reservoir operation on hydrological and geophysical changes from local to regional scales.

Keywords: GRACE, Landsat, Bakun Dam, water storage change, land subsidence, disk load model

1. Introduction

Construction of fresh water reservoir is one of the potential solutions to secure the country development under the risk of climate change and projected increases in population (Ehsani et al., 2017; Ho et al., 2017). However, significant water relocation and impoundment affect the natural hydrological cycle and also likely lead to land subsidence over an extended surrounding area (Graf, 1999; Boy & Chao, 2002). The assessment of the hydrological impact caused by the dam is a general practice, but the accuracy is often limited by a lack of observations (Bierkens et al., 2015). Monitoring the effect using a newly installed ground observation network (e.g., GPS receivers, river gauges) around the construction site is not feasible due to its cost and intensive maintenance requirement. Satellite remote sensing data provide a temporally global coverage measurement, making continuous

monitoring of reservoir water storage and land cover change possible (e.g., Gao et al., 2012; Wang et al., 2011; Zhou et al., 2018). For the land subsidence estimation, in particular, various remote sensing observations are combined to increase the accuracy of the estimate, demonstrated in various applications (e.g., groundwater depletion (e.g., Castellazzi et al. 2016; Hwang et al., 2016), snow accumulation (e.g., Heki, 2001), extreme rainfall (e.g., Bettinelli et al., 2008; Fu et al., 2013) (see Table 1). For the first time, this study utilizes multiple remote sensing data and numerical models to assess the terrestrial water storage (TWS) change and land subsidence caused by the reservoir operation.

[Table 1]

The TWS can be defined as the summation of several storage components, e.g., soil moisture, groundwater, snow, canopy, surface water (e.g., lake, river), and commonly expressed as Equivalent Water Height (EWH), describing an equivalent water thickness (e.g., in m) of a unit area. The TWS can be estimated both from land surface models (LSM) and satellite gravimetry observations (e.g., Syed et al., 2008). The LSMs, forced by precipitation and meteorology, estimate TWS using a sophisticated water and energy balance representation, and have been successfully used to assess the regional water resources in numerous applications (e.g., Koirala et al., 2013; Mo & Lettenmaier, 2013; Wu et al., 2014). The recent LSM development begins to include the representation of groundwater flow (e.g. Niu et al., 2007, Vergnes et al., 2012), anthropogenic water use, including dam operations (Felfelani et al., 2017, Döll et al., 2015), in a multi-physics framework (Yang et al., 2011). However, while adequately representing the natural environment, a majority of LSMs often fail to represent the anthropogenic terms in a highly regulated or controlled environment (e.g., Tatsumi & Yamashiki, 2015; Wang et al., 2011). In such conditions, remotely sensed observation of the TWS derived from the satellite gravimetry observation is the far better alternative. The water (or mass) change produces an anomaly of the Earth's gravity field and such a signal can be observed by the Gravity Recovery And Climate Experiment satellites (GRACE; Tapley et al., 2004). GRACE provides monthly Earth's gravity field variations in terms of the spherical harmonic coefficient (SHC) and had been used to estimate the ΔTWS during its 2002 – 2016 lifetime (e.g., Han et al., 2017;

Lettenmaier & Famiglietti, 2006; Zhou et al., 2018). In contrast to LSM, GRACE observes the entire water column, including all natural and anthropogenic processes, leading to a more complete and accurate record of the estimated ΔTWS. Another advantage of GRACE is the sensitivity associated with mass concentration. A gravity signal of a concentrated mass over a small area can be recovered (Castellazzi et al. 2016), demonstrated by, e.g., Longuevergne et al. (2013), Castellazzi et al. (2018), making GRACE a potential measurement for monitoring the storage variability of the local reservoir.

A significant water impoundment during the dam commencement generally induces a displacement of the Earth's surface (Boy & Chao, 2002). The displacement can be computed using the GRACE SHC data together with the load Love numbers (Bevis et al., 2016; Chanard et al., 2014; 2018; Karegar et al., 2018), which has shown a noticeable agreement with GPS records in broad geographical regions, e.g., Amazon River Basin (Davis et al., 2004), Europe (van Dam et al., 2007), Australia (Han, 2016). Due to the limited spatial resolution (or limited maximum harmonic degree, N_{max} in the spectral domain) of GRACE, the approach is only valid when the spatial extent of surface mass change is sufficiently large (e.g., >250 km resolution). However, the GRACE results may be not adequate for determining the mass change of a small spatial scale and the associated elastic surface deformation. Such a phenomenon can be understood as a GRACE truncation error, which commonly leads to a discrepancy between the GRACE and GPS's vertical displacement estimate (e.g., Khan et al., 2010; Nahmani et al., 2012; Wang et al., 2017). The limitation of GRACE SHC motivates the use of the disk load model in the computation of the local land surface deformation over the region much smaller than GRACE's spatial resolution (Wahr et al., 2013).

The disk load model adopts the Earth's elastic and gravitational response concept to determine the effect of the local hydrological load placement (Bevis et al., 2016; Wahr et al., 2013). A point mass load (e.g., reservoir's water) placed on the Earth's surface would induce the surface of the nearby region to subside and move towards the load. The load model is suitable for a small mass extent as the response can be computed to a very high harmonic degree (e.g., 40,000; Bevis et al., 2016; Wang et al., 2012), representing a spatial resolution of several hundred times higher than what GRACE offers.

105 This paper focuses on assessing the hydrological and geophysical impacts of reservoir operation using
106 Landsat (Irons et al., 2012), GRACE, LSMs, and GPS data. The study area is Sarawak, Malaysia,
107 where the Bakun Dam (Sovacool & Bulan, 2011) was commenced in 2010, the period that Landsat,
108 GRACE, and GPS data are all available for evaluation. The outline of this paper follows three main
109 objectives:

110 1) Quantifying the change of water storage, lake level, and lake area caused by water impoundment,

111 2) Assessing the associated land subsidence, using a developed disk load model to increase the
112 accuracy of the surface deformation estimate, and

113 3) Elaborating the importance of incorporating GRACE with multiple data for modeling regional
114 ΔTWS and land subsidence that might be difficult to be accurately estimated by solely relying on the
115 gravity data.

116 These objectives are presented accordingly in the following Methods, Results, and Discussions
117 sections.

118

119 **2. Study site and materials**

120 **2.1. Study area**

121 The Bakun Dam, an embankment dam in Sarawak, Malaysia (Fig. 1), is the largest hydropower dam
122 in Southeast Asia since 2015, supplying ~2,400 MW of electricity to the Malaysian household (Oh et
123 al., 2010). The dam is located on the Balui River, a tributary of the Rajang River, about 37 km
124 upstream from Belaga. The catchment of 14,750 km^2 receives a yearly average rainfall of ~300 – 400
125 cm, which makes it ideally suited for the hydroelectric development (Sovacool & Bulan, 2011). The
126 205m high dam began impoundment in late 2010 and has operated at its proposed capacity since
127 August 2011. The dam created a vast freshwater reservoir, called Bakun Lake, of >600 km^2 (Shirley
128 and Kammen, 2015), equivalent to the size of Singapore (Bujang et al., 2016). The substantial change
129 in the geographical characteristic of Sarawak's rainforest and altered the water quality and natural

flow of the Balui and Rajang river systems is well documented (e.g., Sovacool & Bulan, 2011). However, impoundments of a significant amount of terrestrial water storage (TWS) not only affects the natural hydrological cycle (Guo et al., 2012; Lu & Siew, 2006), but also induces the land surface displacement, which likely presents as a large scale land subsidence over the area (Boy & Chao, 2002; Zerbini et al., 2007). To date, the impact of the Bakun Dam on the water storage change and land deformation has not been assessed. This study intends for the first time to quantify the TWS variation (ΔTWS) and land subsidence induced by the impoundment of the Bakun Lake.

[Fig. 1]

2.2. Landsat data and digital elevation models

The Landsat-7 (L7) and Landsat-8 (L8) Operational Land Imager (OLI) data are used to delineate the inundated area after the flood commencement. The OLI sensor observes the electromagnetic signals from visible to short-wave spectral bands reflected from the Earth's surface. The combination of the observed surface reflectance can be used to evaluate the land cover change, particularly the surface water. The Landsat data are obtained from the Earth Explorer service (https://earthexplorer.usgs.gov), which provides the surface reflectance every 16 days with a spatial resolution of 30 m. The data are corrected for atmospheric effects using the Dark Object Subtraction (DOS1) method (Chavez, 1996). The DOS1 is an image based algorithm, which applies the correction associated with atmospheric scattering, solar zenith angle, and irradiance. The scenes that have severe cloud cover over the Bakun Lake's area are excluded. The surface water is then derived using the Normalized Difference Water Index (NDWI; McFeeters, 1996), which is computed as:

$$NDWI = \frac{Green - NIR}{Green + NIR}, \quad (1)$$

where $Green$ is a green band (band 2 for L7, band 3 for L8), and NIR is a near infrared band (band 4 for L7, band 5 for L8). The unitless NDWI ranges between -1 and 1. A positive value generally represents the open water, while a zero or negative value represents soil and terrestrial vegetation. The

L7 data are used in the NDWI computation prior to June 2013, and the L7 and L8 data are used together between June 2013 and March 2016 (when L8 data are available). Due to limited cloud-free scenes over Bakun Lake, the yearly-averaged NDWI is used for the analysis.

The lake volume can be approximated using a lake filling model associated with the derived NDWI and digital elevation model (DEM). Three DEMs are considered in the lake volume calculation, the Shuttle Radar Topography Mission (SRTM, Rabus et al., 2003), the Advanced Spaceborne Thermal Emission and Reflection Radiometer - Global Digital Elevation Model Version 2 (ASTER-GDEM2, Tachikawa et al., 2011), and the Advanced Land Observing Satellite World 3D - 30 m (AW3D30, Tadono et al., 2015). The 30 m spatial resolution data is obtained from all products.

2.3. GRACE data

The GRACE twin satellites measure variations of the Earth's gravity field every month using a combination of several measurements onboard, e.g., K-band ranging, accelerometer, attitude, and orbital data (Bettadpur, 2012). As the gravity variation at the monthly time scale is dominated by the hydrological mass changes, the GRACE gravity data are often used to compute ΔTWS (Wahr et al., 1998) and the associated (elastic) load deformation (van Dam et al., 2007), allowing the gravity information to be exploited in a wide range of hydrological and geophysical applications (e.g., Han et al., 2017; Liu et al., 2016; Simon et al., 2017). The GRACE monthly SHC data products are produced by different scientific centers (e.g., Bettadpur, 2012; Dahle et al., 2013; Watkins & Yuan, 2014). Sakumura et al. (2014) demonstrated that averaging multiple gravity solutions may reduce the processing-dependent error in the derived gravity solutions and lead to improved ΔTWS estimates. We compute the time series of ΔTWS and load deformation by averaging four different GRACE solutions, the Centre National d'Etudes Spatiales/Groupe de Recherches de Géodésie Spatiale Release 3 Version 3 (CNES/GRGS; Lemoine et al., 2015), the Center for Space Research, The University of Texas at Austin Release 05 (CSR; Bettadpur, 2012), the Jet Propulsion Laboratory Release 05.1 (JPL, Watkins & Yuan, 2014), and the Deutsches GeoForschungsZentrum Release 05 (GFZ; Dahle et al.,

2013). The GRACE uncertainty is defined as the standard deviation across four solutions. The study period is between August 2002 and March 2016.

The CNES/GRGS solution provides the SHC up to the maximum degree and order N_{max} = 80. The solution has been regularized (using a truncated singular value decomposition), and no additional post-processing is needed to reduce the high-frequency noise (Lemoine et al., 2015). The low degree SHC (including degree 1 and C20 coefficients) are constrained using the Starlette and Stella Satellite Raser Ranging (SLR) data. The CNES/GRGS solution removes the short-term atmospheric and non-tidal oceanic variation from their gravity field solution, while such signals remain intact in the GPS measurement. The two data need to be made consistent in terms of signal contents when conducting the comparison between GRACE gravity and GPS displacement data. In this study, the atmospheric and oceanic variation obtained from the CNES/GRGS de-aliasing product is added to the CNES/GRGS GRACE SHC solutions. Furthermore, the CSR (N_{max} = 96), JPL (N_{max} = 90, and 60 for some months), and GFZ (N_{max} = 90) solutions are filtered using the non-isotropic filter DDK5 (Kusche et al., 2009). We obtain DDK5 solutions directly from the International Centre for Global Earth Models (ICGEM, http://icgem.gfz-potsdam.de/home). After retrieving the data, the degree 1 coefficients are restored using the value provided by Swenson et al. (2008) and the C20 coefficient is replaced by the SLR measurements (Cheng and Tapley, 2004). When comparing with the GPS measurement, the de-aliasing atmospheric and oceanic signals provided by the GRACE AOD1B product (Flechtner et al., 2015) are applied to these GRACE data. The monthly averaged SHC is computed by averaging four (CNES/GRGS, CSR, JPL, and GFZ) GRACE products. Then, its long-term mean (computed between 2002 and 2016) is removed from each monthly solution to obtain the monthly SHC variation.

2.4. LSMs-derived ΔTWS

The monthly ΔTWSs derived from different LSMs are also used to assess the effect of the dam. This study uses four publicly accessible LSM outputs, the Global Land Data Assimilation System, NOAH

(GLDAS; Rodell et al., 2004), the National Centers for Environmental Prediction and the Department of Energy Reanalysis-2 (NCEP; Kanamitsu et al., 2002), the European Centre for Medium-Range Weather Forecasts Re-Analysis Interim (ECMWF; Dee et al., 2011), and the Community Atmosphere Biosphere Land Exchange (CABLE; Decker, 2015). In all models, the ΔTWS is mainly composed of the soil moisture component from multiple soil layers (snow water equivalent is zero). GLDAS also includes canopy storage, while CABLE includes canopy and groundwater storages in the ΔTWS calculation. Water storage from neither natural nor artificial lakes like the Bakum Dam reservoir is available in the LSMs.

In this study, CABLE is forced by the forcing data from the GLDAS dataset and the precipitation from the Tropical Rainfall Measuring Mission (TRMM; Huffman et al., 2007) to increase the model accuracy, as described in Tangdamrongsub et al. (2018). The ensemble open-loop run is performed to obtain the LSM-derived TWS uncertainty. Selected forcing data and model parameters are perturbed by random white noises with 10% of their nominal values (see Tangdamrongsub et al., 2018). The number of ensemble is 100. The model is run independently for each ensemble, and the TWS standard deviation (across all ensemble) is used as the TWS error.

2.5. GPS measurements

The GPS records at station BIN1 (Fig. 1a) are obtained from two data processing centers, the University of Nevada, Reno (UNR), and the University of La Rochelle Analysis Center Consortium (ULR). The UNR solution between September 2007 and March 2016 is obtained from http://geodesy.unr.edu/index.php (Blewitt et al., 2018). The ULR version 6 (ULR6; Santamaría-Gómez et al., 2017) provided a shorter time series, between September 2007 and November 2013, and is downloaded from http://www.sonel.org/-GPS-.html. Other GPS stations located near the Bakun Dam (<150 km) are not used due to the significant data gap and short time span of the records. The monthly averaged value of all three components (up, north, east) is then computed from the daily time series. To reduce the plate tectonic effect (e.g., Fu and Freymueller (2012); Wang et al. (2017)), the

associated long-term trend of up, north, and east component is firstly fitted (using Eq. (A1)) and removed from its time series. Finally, the long-term mean is subtracted from the time series to obtain the variation of the GPS position.

3. Methods

The processing workflow is shown in Fig. 2. The satellite images obtained from Landsat 7 and 8 are used to delineate the Bakun Lake's extent as well as to approximate the lake's level. GRACE data and LSMs are used to estimate the ΔTWS, and the comparison between GRACE and LSMs results is conducted to evaluate a unique benefit of GRACE data in the controlled environment. A forward modeling of the GRACE-derived ΔTWS anomaly during the water impoundment period is also performed to approximate the water level. The lake's outline obtained from Landsat and the lake's level estimated from the GRACE forward modeling are then used to construct the disk load model. The land subsidence is assessed from the disk load model and the GRACE SHC estimate, and the comparison between both results together with the GPS records will confirm the effectiveness of the disk load model application over the Bakun Lake.

[Fig. 2]

3.1 Estimation of lake area and volume from Landsat data

The averaged water level in the Bakun dam after its full operation (e.g., after 2011) can be approximated using the flood simulated model associated with the Landsat-derived NDWI. The general approach is to impound a certain amount of water into the study area (characterized by DEM), and evaluate the water level that produces the same flood extent observed by Landsat (Musa et al., 2015; O'Grady et al., 2011). The GRASS GIS function *r.lake* (https://grass.osgeo.org/grass70/manuals/r.lake.html) is then used to simulate the flood extent associated with a given water level. A range of water levels is tested, and the optimal water level of

the Bakun Lake is chosen when it yields the maximum critical success index (CSI; Roebber, 2009). The CSI is computed as:

$$CSI = \frac{\sum_{i=1}^{K} A}{\sum_{i=1}^{K} (A + B + C)}, \quad (2)$$

where i is the Landsat pixel's index, K is the number of total pixels, and

$$A = \begin{cases} 1; \text{ simulated and observed pixels both identify water} \\ 0; \text{ otherwise} \end{cases},$$

$$B = \begin{cases} 1; \text{ simulated pixels detect water, but no water in observed pixels} \\ 0; \text{ otherwise} \end{cases},$$

$$C = \begin{cases} 1; \text{ simulated pixels fail to detect water} \\ 0; \text{ otherwise} \end{cases}.$$

The CSI values vary between 0 and 1 where 1 indicate that the simulated water level produces an identical flood extent as the observation.

The accuracy of derived NDWIs is assessed using a referenced image from the Earth Science Data Records of Global Forest Cover and Change (ESDR-GFCC, Feng et al., 2016). The ESDR-GFCC derives the percentage of forest cover change in ~5 year-window from the Global Land Survey (GLS) data, and provide the product at 30 m resolution. The 1990, 2000, 2005, 2010, and 2015 products are available, but only the 2015 scene captures the Bakun Lake, and it is used as a reference here. Over the Bakun Lake, the surface water pixel is defined as zero percent forest cover change. To resemble the 2015 ESDR-GFCC scene, we compute the percentage of water pixel change from the derived NDWIs between 2013 and 2016, and the pixel with a zero percent change is defined as surface water. The overall accuracy is computed as $(H + M)/N$, where H is 1 when the NDWI result and reference both detect water (H = 0, otherwise), M = 1 when both miss detecting water (M = 0, otherwise), and N is the number of considered pixels.

3.2 Estimation of ΔTWS and surface deformation from GRACE data

The monthly GRACE product, together with load Love numbers (Bevis et al., 2016; Wang et al., 2012), is used to compute the ΔTWS (Wahr et al., 1998) and the 3D-displacement (van Dam et al., 2007; Wang et al., 2017) caused by the mass load variation as follows:

$$\Delta TWS(\theta,\phi) = \frac{a\rho_{ave}}{3\rho_w}\sum_{n=1}^{N_{\max}}\sum_{m=0}^{n}\bar{P}_{nm}(\cos\theta)(\Delta\bar{C}_{nm}\cos(m\phi)+\Delta\bar{S}_{nm}\sin(m\phi))\frac{2n+1}{1+k_n} \quad (3)$$

$$\Delta r(\theta,\phi) = a\sum_{n=1}^{N_{\max}}\sum_{m=0}^{n}\bar{P}_{nm}(\cos\theta)(\Delta\bar{C}_{nm}\cos(m\phi)+\Delta\bar{S}_{nm}\sin(m\phi))\frac{h_n}{1+k_n} \quad (4)$$

$$\Delta n(\theta,\phi) = -a\sum_{n=1}^{N_{\max}}\sum_{m=0}^{n}\frac{\partial}{\partial\theta}\bar{P}_{nm}(\cos\theta)(\Delta\bar{C}_{nm}\cos(m\phi)+\Delta\bar{S}_{nm}\sin(m\phi))\frac{l_n}{1+k_n} \quad (5)$$

$$\Delta e(\theta,\phi) = \frac{a}{\sin\theta}\sum_{n=1}^{N_{\max}}\sum_{m=0}^{n}\bar{P}_{nm}(\cos\theta)(-\Delta\bar{C}_{nm}\sin(m\phi)+\Delta\bar{S}_{nm}\cos(m\phi))\frac{ml_n}{1+k_n} \quad (6)$$

where $(\Delta r, \Delta n, \Delta e)$ are the displacement of the Earth's surface (meter) in the radial (up), north, and east directions, (θ,ϕ) are the colatitude and east longitude (radian), (k_n, h_n, l_n) are the load Love numbers of degree n (unitless), $\bar{P}_{nm}$ is the normalized associated Legendre function of the first kind of degree n and order m (unitless), (ρ_{ave}, ρ_w) are the average density of the Earth and freshwater (kg/m^3), a is the radius of the Earth (meter), and $(\Delta\bar{C}_{nm}, \Delta\bar{S}_{nm})$ are the monthly SHC variation (unitless). The load Love numbers associated with REF seismological model are used in this paper (Kustowski et al., 2007; Bevis et al.,2016).

3.3 Derivation of lake's water level using TWS forward model

The forward model ($\boldsymbol{f}$) associated with the GRACE-derived ΔTWS can be used to determine a water level of the Bakun Lake. The lake basin function ($\boldsymbol{b}_D$) is firstly designed by setting a value of a uniform water level (D) in the lake while setting outside value as zero. Then, the Gaussian smoothing (G) is applied to the basin function ($\boldsymbol{f} = G(\boldsymbol{b}_D)$) to simulate the water storage at the GRACE spatial resolution. The variance ratio, $v = \sum_i^K(\boldsymbol{d}_i - \boldsymbol{f}_i)^2/\boldsymbol{d}_i^2$ (i is the considered grid cell, and K is the

number of grid cells), is used to find the optimal water level parameter D from the GRACE observation ($\boldsymbol{d}$). The spatial resolution of GRACE is obtained from the correlation length, estimated from the empirical covariance function $C(\psi)$ (see Eq. (3 – 5) of Tscherning and Rapp, 1974), where ψ is the spherical distance. The correlation length is defined as the distance (ψ) where the $C(\psi = 0)$ decreases by half.

It should be noted that the GRACE-derived (equivalent) water level variation includes all hydrological components, e.g., surface water, soil moisture, groundwater, and the estimate might be different from the measured reservoir level (e.g., from gauge data) that reflects only the surface water component.

3.4 Development of disk load model

The disk load is designed as a cylinder with a given radius and thickness. A number of discrete loads are placed along the outline of the water body (e.g., delimited from the satellite imagery data), and the total displacement is computed by summing the contributed responses from all disk loads. Following this concept, the surface mass load (σ, kg/m^2) as a function of the angular distance (φ, radian) away from the load center can be formulated based on a series of Legendre polynomials as follows:

$$\sigma(\varphi) = \sum_{n=0}^{N_{\max}} \sigma_n P_n(\cos\varphi)\,, \tag{7}$$

and the disk load coefficient σ_n (kg/m^2) is computed as (Bevis et al., 2016; Wahr et al., 2013):

$$\sigma_n = \frac{\rho_w D}{2}\begin{cases} (1-\cos\alpha) & n = 0 \\ -P_{n+1}(\cos\alpha) + P_{n-1}(\cos\alpha) & n \geq 1 \end{cases}, \tag{8}$$

where α is the angular disk radius (radian), P_n is the Legendre polynomial of degree n (unitless), and D is the disc thickness (meter), which is defined as a water depth in this study. The vertical (V) and horizontal (H) displacements (meter) caused by the disk load are formulated as:

$$V(\varphi) = \frac{4\pi a^3}{M_e} \sum_{n=0}^{N_{\max}} \frac{\sigma_n h_n}{2n+1} P_n(\cos\varphi), \quad (9)$$

$$H(\varphi) = \frac{4\pi a^3}{M_e} \sum_{n=0}^{N_{\max}} \frac{\sigma_n l_n}{2n+1} \frac{\partial}{\partial\varphi} P_n(\cos\varphi), \quad (10)$$

where M_e is the mass of the Earth (kg). $V(\varphi)$ is measured upward, while $H(\varphi)$ is measured in the direction of increasing angular distance. The uncertainties of $V(\varphi)$ and $H(\varphi)$ are calculated by using an error propagation (see, e.g., Eq. (15) of Tangdamrongsub et al. (2017)).

4. Results

4.1 Inundated area and lake volume from Landsat data

The yearly average NDWIs derived from the Landsat data between 2007 and 2016 are shown in Fig. 3. After a careful inspection, we found that the NDWI values greater than 0.2 represent the surface water, while the values <0.1 generally include clouds and vegetation. Therefore, we define a surface water pixel for NDWI > 0.2 as a safe threshold. The derived NDWI has an overall accuracy of ~95 % evaluating against the ESDR-GFCC data (Sect. 3.1). We found that the accuracy is reduced when the NDWI threshold is smaller than 0.2, which is likely caused by the contamination of cloud and vegetation pixels in the calculation. From Fig. 3, the distinct layouts of the Rajang and Balui Rivers are seen between 2007 and 2010 (and also before 2007, not shown), but no sign of the Bakun Lake is observed (Fig. 3a – d). The expansion of the inundated area is clearly visible in 2011 when the Bakun Dam began its operation (Fig. 3e), and the lake extent has no significant change from 2012 onward (Fig. 3f – j). The averaged NDWI between 2012 and 2016 is then used to delineate the lake boundary (polygon). The inundated area can be calculated by integrating the area of all water pixels inside the lake polygon, as shown in Fig. 3k. The inundated area is substantially increased by 12 times (from ~50 km^2 before 2011 to ~600 km^2 after 2012).

[Fig. 3]

346 The Landsat data and DEM are used to approximate lake volume. The water pixels derived from the
347 averaged NDWI between 2012 and 2016 is defined as the observation (Fig. 4a). Figs. 4b – d
348 demonstrate the simulated inundated area after filling the lake area with the averaged water levels of
349 approximately 46 m, 60 m, and 73 m, respectively. With increasing water level, the flood firstly
350 emerges around the downstream of the Balui River and progresses upstream through Rumah Baka and
351 Rumah Kulit, respectively. The maximum CSI value is obtained when the simulated water level of ~
352 75 m (corresponding to 48 Gt of total water mass) is used (Fig. 5), and it results in the best agreement
353 with the observed flood extension (Fig. 4a). Comparing with SRTM, the average water level is
354 reduced by ~ 2m, and increased by ~1 m when AW3D30 and ASTER-GDEM2 are used, respectively.
355 The difference is ~ 1.5 m or 1.8 % of the approximate water level.

356 *[Fig. 4]*

357 *[Fig. 5]*

358 **4.2 GRACE-derived ΔTWS and water level changes**

359 The GRACE-derived ΔTWS of the Bakun Dam (averaged ΔTWS inside the flood polygon) between
360 2002 and 2016 is shown in Fig. 6. The time series are fitted with six variables to estimate the long-
361 term, annual amplitude, and phase (see Appendix A). The ΔTWS time series shows a slightly
362 increasing trend of ~ 2 mm/year and a seasonal amplitude of ~ 16 mm (Table 2) before the flood
363 commencement. On average, the ΔTWS's standard deviation between 2002 and 2016 is ~52 mm. The
364 water impoundment signature is clearly seen from August 2010, and the ΔTWS is significantly
365 increased by approximately 200 mm (equivalent water height) between August 2010 and December
366 2011. Therefore, we define the period of August 2010 – December 2011 as the impoundment period
367 in this study. The ΔTWS has been steady since 2012, with a similar trend (~2 mm/year) but with
368 twice the seasonal amplitude, ~38 mm. This reflects the role of the Bakun Dam in transiently storing
369 water during the wet season (and reducing runoff) to release during the dry season (e.g.,
370 Longuevergne et al. 2013). It is also observed that there is a change in the seasonal peak TWS
371 occurrence from December to February, after the dam construction, which is likely caused by the

retention time of the reservoir. The reservoir fill and release regulation are made to spill excess capacity and to maintain some level of flow in the river downstream of the dam. In addition, the El Niño/Southern Oscillation (Wang et al., 2000) signature is seen in the ΔTWS before the flood commencement. The 2009 El Niño (less precipitation in South-East Asia) is the main cause of the low ΔTWS in summer 2009 (Han et al., 2017). The ENSO effect on the ΔTWS is less pronounced in the Bakun Dam area compared to the central and southern parts of Kalimantan (southern part of the island), where the peat fire also likely intensifies the water storage loss (Han et al., 2017).

[Fig. 6]

[Table 2]

The spatial pattern of GRACE ΔTWS change between the pre-dam (August 2002 – July 2010) and post-dam (January 2012 – March 2016) periods is computed and shown in Fig. 7a. The increased ΔTWS of ~200 mm is found around the Bakun Lake. The decreased ΔTWS in the southern part of the island is likely caused by the decreased rainfall after 2012 (Han et al., 2017). We apply the TWS forward model to approximate the water level of the Bakun Dam, by using the ΔTWS difference (Fig. 7a) as the observation and evaluate the forward model's result associated with given uniform water levels ranging between ~100 m and ~140 m height with respect to the base of the dam. The smoothing radius of the forward model is obtained from the ΔTWS correlation length estimate. The averaged covariance functions computed using the GRACE-derived ΔTWS between August 2002 and March 2016 from all GRACE solutions (CSR, JPL, GFZ, CNES/GRGS, and average) presents a very similar feature, and the correlation length of ~275 km is found in all solutions (Fig. 7b). The forward model shows a similar spatial feature to the observation around the dam location (Fig. 7c), and its intensity is proportional to the parameter D. Considering only the averaged ΔTWS inside the Bakun Lake, the minimum variance ratio (v) is found when $D \approx 120$ m (Fig. 7d). We assume that the error of GRACE-derived ΔTWS follows a normal distribution (described by zero mean and standard deviation of 52 mm), and the uncertainty of the approximate water level is estimated based on an error propagation method. This corresponds to the water level uncertainty of ~27 m. The TWS forward modeling approach is applied to all monthly GRACE-derived ΔTWS to approximate the water level variations

of the Bakun Lake, and the water level time series is displayed in Fig. 2 (associated with the right axis).

[Fig. 7]

4.3 LSMs-derived ΔTWS

The ΔTWS estimates of the Bakun Dam simulated from four different LSMs are shown in Fig. 8a. All models show an increasing long-term trend in the pre-dam period (Table 2). The CABLE and GLDAS models show an increasing trend of approximately 3 – 4 mm/year, consistent with the value observed by the GRACE observation. The NCEP and ECMWF models show a significantly larger trend estimate of ~16 mm/year, mainly due to the significantly low ΔTWS between 2002 and 2005 influenced by the exceptionally low rainfall (Fig. 8b). In the post-dam period, in contrast to GRACE, the negative trends are observed from all models, which is mainly induced by the reduction of rainfall after 2008. None of the LSMs adequately captures the GRACE signals of ΔTWS increase associated with the Bakun Dam water storage. A seasonal variation during the post-dam period is observed in CABLE and GLDAS with the twice increased annual amplitude (compared to the pre-dam period). The increased precipitation is responsible for an increased wet condition, which is in favor of the water storing operation (see Sect. 4.2). By contrast, NCEP and ECMWF do not present any significant change in the seasonal variation over time. No significant change in the seasonal timing is observed from all models.

[Fig. 8]

The spatial patterns of the ΔTWS difference (post-dam minus pre-dam) are computed from LSMs (see Sect. 4.2) and shown in Figs. 8c – 8f. The precipitation differences corresponding to each LSM are also computed in the same manner and shown in Figs. 8g – 8j. It is found that the spatial patterns of the modeled ΔTWS are consistent with the associated precipitation data (Figs. 8g – 8j), not with GRACE observations (Fig. 7a).

The modeled ΔTWS is evaluated in terms of temporal correlation against the GRACE observation, and the correlation coefficients associated with different LSMs (with 0.05 significant level) are shown in Table 3. The cross-correlation among four LSMs shows that only two out of six pairs are in agreement; for example, the correlation greater than 0.7 for the pairs of CABLE vs. GLDAS and NCEP vs. ECMWF. The correlation between CABLE (or GLDAS) and NCEP (or ECMWF) is as low as 0.22, indicating the high uncertainty of the LSM simulated ΔTWS in this area. As expected, all models are poorly correlated with the GRACE observations. Absent to consider the Bakun Dam's effect in the TWS calculation likely leads to an inaccurate ΔTWS estimate, which makes the current LSM simulation less favorable for the water resource assessment or the hydrological reanalysis application in this region.

[Table 3]

During the reservoir impoundment, the impounded water is first distributed through the soil and groundwater zones, filling pore space until the maximum saturated TWS capacity is reached, and the exceeded capacity results in surface water. The required filling capacity (before the appearance of the lake) can be approximated by CABLE, whose land cover parameters are publicly accessible. We found that the CABLE-estimated TWS between January 2010 and July 2010 (period prior to impoundment) is stable at ~10.40 ± 0.35 m, which is lower than the saturated capacity by ~0.83 m. Note that the obtained value is at the model resolution. We compute the required filling capacity at the Bakun Lake by applying the TWS forward model in a similar manner as GRACE and obtained the water level of ~ 34 ± 7 m that needs to be filled as a foundation of the Bakun Lake.

The summation between the Landsat-derived lake level (75 ± 1.5 m) and the required filling capacity (34 ± 7 m) shows a reasonable agreement with the water level approximated by GRACE (109 ± 7 m Vs. 119 ± 27 m).

4.4 Land subsidence

449 The solid Earth deforms elastically in response to surface water load (Farrell, 1972). An elastic Earth
450 model is taken to compute the three-dimensional surface deformation induced by the Bakun Lake load
451 using the GRACE (truncated) SHC data as well as the disk load model of the reservoir. The disk
452 model is essentially determined with Landsat inundated area and constrained by GRACE-derived
453 ΔTWS for water level changes, as described previously. The Bakun Lake load is spatially localized
454 demanding spherical harmonic expansion to the degree considerably higher than what GRACE data
455 provide.

456 The Bakun Lake disk model is composed of multiple disks with variable radii covering the flooded
457 area, as shown on the inset map in Fig. 9a. The total area of the disk loads is ~600 km^2, corresponding
458 to the area derived from the Landsat data (Sect. 3.1). The averaged monthly water level derived from
459 GRACE is used to constrain monthly changes of uniform thickness of the Lake disks (Sect. 3.3). The
460 vertical displacement is calculated from the disk model using Eq. (9) with $N_{\max} = 40{,}000$, and the
461 result is shown in Fig. 9a. It is seen that significant subsidence (~200 mm) occurs beneath the lake a
462 result of the elastic deformation with the lake load and the amount of subsidence rapidly decreases
463 with distance from the lake. The subsidence is computed to be around ~9 mm at GPS site BIN1. The
464 vertical displacement is also computed using the GRACE SHC data using Eq. (4). The difference in
465 the GRACE-derived vertical displacement between the pre-dam and post-dam period is shown in Fig.
466 9b. The subsidence derived from the GRACE SHC data is markedly smaller than the disk model (e.g.,
467 ~3 mm vs. ~200 mm around the lake) due to truncation of GRACE SHC data. The load deformation
468 signal spreads (leaks) over a wider area around the lake resulting significantly smaller subsidence at
469 the BIN1 site. Such leakage effect is considerable if the source load is spatially confined.

470 *[Fig. 9]*

471 The displacement computed with the truncated GRACE SHC data is substantially underestimated due
472 to the localized nature of the load (only over 600 km^2). The effect of the truncated GRACE data is
473 demonstrated as follows. Two disk loads with the same mass (0.7 Gt) are assumed; one with 150 km
474 radius and 1 cm depth (Disk 1), and the other with 15 km radius and 1 m depth (Disk 2). We compute
475 the vertical displacements of Disk 1 and Disk 2 with different $N_{\max}$ (90 and 40,000) using Eqs. (7 –

476 10), and the results are shown in Fig. 10. The vertical displacements of Disk 1 with different $N_{\max}$ are
477 similar, and the ratio (β) between the deformations associated with $N_{\max} = 40{,}000$ and $N_{\max} = 90$ at
478 the disk's center is 1.2. By contrast, the truncation degree plays a significant role for Disk 2. The
479 vertical displacement at the center of the disk increases with $N_{\max}$, and converges at $N_{\max}$~3,000
480 (not shown), which agrees with the rule of thumb given in Bevis et al. (2016). The β value of Disk 2
481 is 17.9. It is also seen that the vertical load deformation by Disk 1 and Disk 2 are roughly similar at
482 the GRACE resolution ($N_{\max}$~90). This example demonstrates that the ground displacements
483 computed with GRACE (truncated) SHC data can be significantly underestimated for the case of
484 spatially localized load (like Disk 2), while the GRACE computation of the load deformation is still
485 acceptable for the broad scale load (like Disk 1).

486 *[Fig. 10]*

487 Different choices of disk thickness and earth models have little impact on the estimated land
488 subsidence at BIN1 station. To demonstrate this, we compute the deformation from the disk model
489 constructed using 1) various disk thickness obtained from lake filling model (Sect. 4.3), and 2)
490 uniform thickness obtained from the averaged lake level. The spatial pattern of two different load
491 distributions is very similar (Fig. 11). Only a slight difference is seen near the upstream of the Bakun
492 Lake (Fig. 11a, b). The deformation profile between the BIN1 station (point A) and the Bakun Dam
493 (point B) shows a clear difference near the Bakun Dam, but hardly noticeable beyond 10 km away
494 from the lake (Fig. 11c).

495 *[Fig. 11]*

496 To assess the impact of the Earth's model, various sets of Load Love Numbers (Bevis et al., 2016;
497 Wang et al., 2012) are applied to the disk load model, and the estimated vertical deformation between
498 the BIN1 station (point A in Fig. 11) and the Bakun Dam (point B in Fig. 11) are shown in Fig. 12.
499 Similar to Fig. 10c, the difference is noticeable near the Bakun Lake, where PREMsoft model
500 produces the greatest subsidence, and PREMhard produces the smallest. The estimated deformations

501 are converged after ~40 km away from the lake, and the effect of using different Earth's model is
502 trivial at BIN1 station. Wang et al. (2012) and Wahr et al. (2013), also report similar behavior.

503 *[Fig. 12]*

504 The computed vertical displacements from the disk load model and the GRACE SHC data are
505 compared with the GPS measurements at the BIN1 station after the long-term mean is removed (Fig.
506 13). The total subsidence is measured by two GPS solutions; GRACE, and the disk model, as shown
507 in Table 4. The total change is calculated by multiplying the estimated linear trend between August
508 2010 and December 2011 (see the displayed slopes in Fig. 13) with the impoundment period (e.g., 17
509 months). The GPS data present that the BIN1 station indicates subsidence of approximately 10 – 11
510 mm (or about 7 – 8 mm/year) during the impoundment period. The GPS solutions show a significant
511 agreement, with correlation value (ρ) of 0.9 (Fig. 14). The disk model is consistent with the GPS time
512 series (~ 9 mm subsidence with ρ = 0.77). Due to SHC truncation, the GRACE-derived vertical
513 displacement shows 6 – 7 times smaller deformation at BIN1, and the ρ value is approximately 13 %
514 lower than the disk model.

515 *[Fig. 13]*

516 *[Table 4]*

517 *[Fig. 14]*

518 The horizontal displacements computed from the disk load model and the GRACE SHC data are
519 compared with the GPS measurements (Fig. 15). The disk load model predicts the deformation
520 southward by ~2.4 mm and eastward by ~3.3 mm (see Table 4), or 4.1 mm toward the Bakun Lake
521 during the impoundment period (Fig. 16). The motion of the GPS-ULR solution shows a reasonable
522 agreement with the disk load model or 3.8 mm toward the lake. The GPS-UNR solution only agrees
523 with the disk load model (and the GPS-ULR solution) in the north component, while it moves away
524 from the lake in the east-west direction (Fig. 15c). It is unclear why the east component of the GPS
525 time series is less consistent between two solutions. The inconsistent use of reference frame,
526 tropospheric model, and GPS orbit and clock could be responsible for such difference. The GRACE

SHC data fails to capture the elastic deformation by the lake load due to the omission error. Instead, the computed deformation from GRACE SHC data is likely the deformation caused by the seasonal migration of degree-1 load (geocenter motion), as also seen in Han (2016). The GPS horizontal measurements also present the coherent seasonal motions synchronized with the GRACE results.

[Fig. 15]

[Fig. 16]

5. Discussion

The satellite images obtained from Landsat 7 and 8 observe the flooded area expanded up to 600 km^2 between 2010 and 2011. The increased surface water area and water storage are caused by the artificial reservoir after the construction of the Bakun hydroelectric dam downstream of the Balui River. The increased water mass estimated from the Landsat image and DEM data analysis is approximately 48 Gt. The results obtained from remote sensing data are in line with the estimated lake area (594 – 695 km^2) and gross storage capacity (~44 Gt) reported by the Sarawak integrated water resources management master plan (e.g., Sovacool & Bulan, 2011; Shirleym & Kammen, 2015). In the same period, GRACE observes the increased mass change northwest (Malaysian part) of the Borneo island by ~200 mm in equivalent water height. This is 2-3 times larger than the seasonal water storage change predicted by the LSMs, which do not include the Bakun lake storage but are constrained principally by soil moisture and groundwater storages. We find the corresponding water level of ~120 m increasing during the impoundment, which is the composite of surface water (70 %) and underground water components (30 %). In total, GRACE observes ~71 Gt of fresh water that has been stored in the Bakun Lake since 2011. This is comparable to nearly twice the annual ice mass loss in Alaska glacier and more than the total annual loss of the western Antarctica ice sheet (Bamber, 2018).

Our developed disk load model of the Bakun Lake constrained by the GRACE and Landsat data predicts land subsidence about 200 mm at the lake and ~9 mm around the nearby coastal area. The

553 magnitude of the subsidence is around twice the global mean sea level rise trend (Chen et al., 2017).
554 As such, the relative sea level rise near the west coastal Borneo is supposed to be tentatively 2-3 times
555 faster during the impoundment period, and the impoundment effect should be considered in the
556 estimation of the sea level variation in the coastal zones (Nicholls and Cazenave, 2010). Such load
557 displacement estimate is in a good agreement with the actual GPS records at the coastal town Bintulu
558 (BIN1). The reservoir impoundment causes the GPS site to move toward the lake by ~4 mm, observed
559 from the disk load model and GPS-ULR solution. The magnitude of the horizontal displacement is
560 approximately two to three times smaller than the vertical component, which is in line with the
561 finding of Wahr et al. (2013). We emphasize here that the subsidence estimate of the Bakun Lake is
562 the result of the elastic response. Subsidence process could link to an inelastic response of Earth
563 material, e.g., a variation of aquifer system (Amelung et al. 1999; Erban et al., 2014), and our
564 approach is unlikely suitable for such an application.

565 This study presents a framework for merging the strength of multiple remote sensing data and
566 numerical modeling sources. The advantage and limitation of different data learned from this study
567 are summarized in Table 5. GRACE possesses a clear strength of observing the total mass variation
568 that cannot be captured by other observations. However, the direct use of GRACE data cannot provide
569 a complete gravity signal due to the truncation of SHC. The effect is severe for a load associated with
570 short wavelength, which can cause systematic misfits with the validated data (e.g., Fig. 11, see also Fu
571 et al., 2013). A numerical model can be developed to utilize the strength of GRACE and Landsat data
572 in an iterative manner and is used to recover the full spectral band of the gravity signal. As a result,
573 GRACE is capable of detecting a variability of localized mass distribution over the area as small as
574 600 km^2. The size of this area is considered the smallest for which GRACE has been utilized for
575 hydrological application, e.g., ~10 times smaller than Lake Nasser (Longuevergne et al., 2013), and
576 Lake Urmia (Tourian et al., 2015). However, the mass variability of the Bakun Lake is as large as (or
577 larger) than Lake Nasser and Lake Urmia, which explains the sensitivity of GRACE over the Bakun
578 Lake. The size of mass variation (Gt) plays a major role in GRACE application, which is also

described in e.g., Longuevergne et al. (2013), Tourian et al. (2015), Yi et al. (2017), Castellazzi et al. (2018), Mu et al. (2019).

6. Conclusion

We developed and demonstrated a technique to quantify the total water storage change and land subsidence caused by the impoundment of the Bakun Lake. The lake area variability is derived from the high-resolution Landsat imagery data. The effective lake water level is determined using GRACE data through a developed forward model. The land subsidence is then estimated by incorporating Landsat and GRACE strengths into the developed disk load model, and the results are consistent with the GPS measurement.

Recovering the local water storage is difficult using the GRACE data alone. This study demonstrates how the low-resolution GRACE-derived ΔTWS data can be successfully used to determine and model the surface water load over an area considerably less than the GRACE's intrinsic resolution, in conjunction with high-resolution Landsat image data. Our approach provides the opportunity to extract the local hydrological or geophysical signals that are still hidden in the GRACE observation, allowing the utilization of the GRACE data in broader applications. The impoundment of the Bakun Dam can be used as a large-scale natural experiment to test the current understanding of the water cycle under anthropogenic pressure, ability to capture mass changes with geodetic tools and propose how models could be improved.

Acknowledgment

This work was funded by the NASA Earth Science Division in support of the National Climate Assessment. This work was also supported partially by the University of Newcastle to support NASA's GRACE and GRACE Follow-On projects as a science team member to the missions and by Australian Research Council Discovery Program (grant no. DP170100224). We gratefully thank for

all valuable suggestions from Tim R. McVicar, Manoochehr Shirzaei, Laurent Longuevergne, two anonymous reviewers, and RSE editorial team, which help us improve the manuscript significantly.

Appendix A: Estimation of annual amplitude and phase of time series

The time series is represented by

$$L = f_0 + f_1 t + f_2 sin(\omega t) + f_3 cos(\omega t) + f_4 sin(2\omega t) + f_5 cos(2\omega t) \quad , \qquad \text{(A1)}$$

where L is the vector containing observations, t is the observation time, and $\omega = 2\pi/T$ with T the annual period. The coefficients $f_0, \dots, f_5$ are estimated using least-squares adjustment. The annual amplitude (A) is estimated as

$$A = \sqrt{f_2^2 + f_3^2} \quad , \qquad \text{(A2)}$$

and the phase (φ) is estimated as

$$\varphi = \arctan_2(f_2, f_3). \qquad \text{(A3)}$$

The atan2 returns a value in the range $(-\pi, \pi]$, which can be represented using 12 calendar months (from Jan to Dec).

References

Amelung, F., Galloway, D.L., Bell, J.W., Zebker, H.A., Laczniak, R.J., 1999. Sensing the ups and downs of Las Vegas: InSAR reveals structural control of land subsidence and aquifer-system deformation. Geology 27, 483–486. https://doi.org/10.1130/0091-7613(1999)027<0483:STUADO>2.3.CO;2

Bamber, J. L., Westaway, R. M., Marzeion, B., & Wouters, B. (2018). The land ice contribution to sea level during the satellite era. *Environmental Research Letters, 13, 06.3008*. https://doi.org/10.1088/1748-9326/aac2f0

Bettadpur, S. (2012, May 29). *Gravity Recovery and Climate Experiment UTCSR Level-2 processing standards document for Level-2 product release 0005*. Center for Space Research, The University of Texas at Austin, USA. Available online at: ftp://podaac.jpl.nasa.gov/allData/grace/docs/L2-UserHandbook_v3.0.pdf

Bettinelli, P., Avouac, J.-P., Flouzat, M., Bollinger, L., Ramillien, G., Rajaure, S., Sapkota, S., 2008. Seasonal variations of seismicity and geodetic strain in the Himalaya induced by surface hydrology. Earth and Planetary Science Letters 266, 332–344. https://doi.org/10.1016/j.epsl.2007.11.021

Bevis, M., Melini, D., & Spada, G. (2016). On computing the geoelastic response to a disk load. *Geophysical Journal International*, *205*(3), 1804–1812. https://doi.org/10.1093/gji/ggw115

Bierkens, M.F.P., Bell, V.A., Burek, P., Chaney, N., Condon, L.E., David, C.H., Roo, A. de, Döll, P., Drost, N., Famiglietti, J.S., Flörke, M., Gochis, D.J., Houser, P., Hut, R., Keune, J., Kollet, S., Maxwell, R.M., Reager, J.T., Samaniego, L., Sudicky, E., Sutanudjaja, E.H., Giesen, N. van de, Winsemius, H., Wood, E.F., 2015. Hyper-resolution global hydrological modelling: what is next? Hydrological Processes 29, 310–320. https://doi.org/10.1002/hyp.10391

Blewitt, G., Hammond, W. C., Kreemer, C. (2018). Harnessing the GPS Data Explosion for Interdisciplinary Science. Eos, 99. https://doi.org/10.1029/2018EO104623.

Boy J.-P. & Chao, B. F. (2002). Time-variable gravity signal during the water impoundment of China's Three-Gorges Reservoir. *Geophysical Research Letters*, *29*(24), 53–1. https://doi.org/10.1029/2002GL016457

Bujang, A. S., Bern, C. J., & Brumm, T. J. (2016). Summary of energy demand and renewable energy policies in Malaysia. *Renewable and Sustainable Energy Reviews*, *53*, 1459–1467. https://doi.org/10.1016/j.rser.2015.09.047

Castellazzi, P., Arroyo-Domínguez, N., Martel, R., Calderhead, A.I., Normand, J.C.L., Gárfias, J., Rivera, A., 2016. Land subsidence in major cities of Central Mexico: Interpreting InSAR-derived land subsidence mapping with hydrogeological data. International Journal of Applied Earth Observation and Geoinformation 47, 102–111. https://doi.org/10.1016/j.jag.2015.12.002

Castellazzi, P., Longuevergne, L., Martel, R., Rivera, A., Brouard, C., & Chaussard, E. (2018). Quantitative mapping of groundwater depletion at the water management scale using a combined GRACE/InSAR approach. Remote Sensing of Environment, 205, 408-418.

Chanard, K., Avouac, J.P., Ramillien, G., Genrich, J., 2014. Modeling deformation induced by seasonal variations of continental water in the Himalaya region: Sensitivity to Earth elastic structure. Journal of Geophysical Research: Solid Earth 119, 5097–5113. https://doi.org/10.1002/2013JB010451

Chanard, K., Fleitout, L., Calais, E., Rebischung, P., Avouac, J.-P., 2018. Toward a Global Horizontal and Vertical Elastic Load Deformation Model Derived from GRACE and GNSS Station Position Time Series. Journal of Geophysical Research: Solid Earth 123, 3225–3237. https://doi.org/10.1002/2017JB015245

Chavez, J. (1996). Image-based atmospheric corrections - Revisited and improved. *Photogrammetric Engineering and Remote Sensing*, *62*(9), 1025–1036.

Chen, X., Zhang, X., Church, J. A., Watson, C. S., King, M. A., Monselesan, D., et al. (2017). The increasing rate of global mean sea-level rise during 1993–2014. *Nature Climate Change*, *7*(7), 492–495. https://doi.org/10.1038/nclimate3325

Cheng, M., & Tapley, B. D. (2004). Variations in the Earth's oblateness during the past 28 years. *Journal of Geophysical Research: Solid Earth*, *109*(B9), B09402. https://doi.org/10.1029/2004JB003028

Dahle, C., Flechtner, F., Gruber, C., Koenig, D., Koenig, R., Michalak, G., & Neumayer, K.-H. (2013). GFZ GRACE Level-2 Processing Standards Document for Level-2 Product Release 0005 : revised edition, January 2013. Deutsches GeoForschungsZentrum (GFZ). https://doi.org/10.2312/gfz.b103-1202-25

Davis, J. L., Elósegui, P., Mitrovica, J. X., & Tamisiea, M. E. (2004). Climate-driven deformation of the solid Earth from GRACE and GPS. *Geophysical Research Letters*, *31*(24), L24605. https://doi.org/10.1029/2004GL021435

Decker, M. (2015). Development and evaluation of a new soil moisture and runoff parameterization for the CABLE LSM including subgrid-scale processes. *Journal of Advances in Modeling Earth Systems*, *7*(4), 1788–1809. https://doi.org/10.1002/2015MS000507

Dee, D. P., Uppala, S. M., Simmons, A. J., Berrisford, P., Poli, P., Kobayashi, S., et al. (2011). The ERA-Interim reanalysis: configuration and performance of the data assimilation system. *Quarterly Journal of the Royal Meteorological Society*, *137*(656), 553–597. https://doi.org/10.1002/qj.828

Döll, P., Douville, H., Güntner, A., Schmied, H. M., & Wada, Y. (2016). Modelling freshwater resources at the global scale: Challenges and prospects. Surveys in Geophysics, 37(2), 195-221.

Ehsani, N., Vörösmarty, C.J., Fekete, B.M., Stakhiv, E.Z., 2017. Reservoir operations under climate change: Storage capacity options to mitigate risk. Journal of Hydrology 555, 435–446. https://doi.org/10.1016/j.jhydrol.2017.09.008

Erban, L.E., Gorelick, S.M., Zebker, H.A., 2014. Groundwater extraction, land subsidence, and sea-level rise in the Mekong Delta, Vietnam. Environ. Res. Lett. 9, 084010. https://doi.org/10.1088/1748-9326/9/8/084010

Farrell, W. E. (1972). Deformation of the Earth by surface loads. *Reviews of Geophysics*, *10*(3), 761–797. https://doi.org/10.1029/RG010i003p00761

Felfelani, F., Wada, Y., Longuevergne, L., & Pokhrel, Y. N. (2017). Natural and human-induced terrestrial water storage change: A global analysis using hydrological models and GRACE. Journal of Hydrology, 553, 105-118.

Feng, M., Sexton, J.O., Huang, C., Anand, A., Channan, S., Song, X.-P., Song, D.-X., Kim, D.-H., Noojipady, P., Townshend, J.R., 2016. Earth science data records of global forest cover and change: Assessment of accuracy in 1990, 2000, and 2005 epochs. Remote Sensing of Environment 184, 73–85. https://doi.org/10.1016/j.rse.2016.06.012

Flechtner, F., Dobslaw, H., & Elisa, F. (2015). AOD1B product description document for product release 05. GFZ German Research Centre for Geosciences.

Fu, Y., & Freymueller, J. T. (2012). Seasonal and long-term vertical deformation in the Nepal Himalaya constrained by GPS and GRACE measurements. *Journal of Geophysical Research: Solid Earth*, *117*(B3). https://doi.org/10.1029/2011JB008925

Fu, Y., Argus, D.F., Freymueller, J.T., & Heflin, M.B. (2013). Horizontal motion in elastic response to seasonal loading of rain water in the Amazon Basin and monsoon water in Southeast Asia observed by GPS and inferred from GRACE. Geophysical Research Letters 40, 6048–6053. https://doi.org/10.1002/2013GL058093

Graf, W.L., 1999. Dam nation: A geographic census of American dams and their large-scale hydrologic impacts. Water Resources Research 35, 1305–1311. https://doi.org/10.1029/1999WR900016

Guo, H., Hu, Q., Zhang, Q., & Feng, S. (2012). Effects of the Three Gorges Dam on Yangtze River flow and river interaction with Poyang Lake, China: 2003–2008. *Journal of Hydrology*, *416–417*, 19–27. https://doi.org/10.1016/j.jhydrol.2011.11.027

Han, J., Tangdamrongsub, N., Hwang, C., & Abidin, H. Z. (2017). Intensified water storage loss by biomass burning in Kalimantan: Detection by GRACE. *Journal of Geophysical Research: Solid Earth*, *122*(3), 2017JB014129. https://doi.org/10.1002/2017JB014129

Han, S.-C. (2016). Seasonal clockwise gyration and tilt of the Australian continent chasing the center of mass of the Earth's system from GPS and GRACE. *Journal of Geophysical Research: Solid Earth*, *121*(10), 7666–7680. https://doi.org/10.1002/2016JB013388

Han, S.-C. (2017), Elastic deformation of the Australian continent induced by seasonal water cycles and the 2010–2011 La Niña determined using GPS and GRACE, Geophys. Res. Lett., 44, 2763–2772, doi:10.1002/2017GL072999.

Heki, K., 2001. Seasonal Modulation of Interseismic Strain Buildup in Northeastern Japan Driven by Snow Loads. *Science*, *293*, 89–92. https://doi.org/10.1126/science.1061056

Ho, M., Lall, U., Allaire, M., Devineni, N., Kwon, H.H., Pal, I., Raff, D., Wegner, D., 2017. The future role of dams in the United States of America. *Water Resources Research 53*, 982–998. https://doi.org/10.1002/2016WR019905

735 Huffman, G. J., Bolvin, D. T., Nelkin, E. J., Wolff, D. B., Adler, R. F., Gu, G., et al. (2007). The
736 TRMM Multisatellite Precipitation Analysis (TMPA): Quasi-Global, Multiyear, Combined-
737 Sensor Precipitation Estimates at Fine Scales. *Journal of Hydrometeorology*, *8*(1), 38–55.
738 https://doi.org/10.1175/JHM560.1
739 Hwang, C., Yang, Y., Kao, R., Han, J., Shum, C.K., Galloway, D.L., Sneed, M., Hung, W.-C., Cheng,
740 Y.-S., Li, F., 2016. Time-varying land subsidence detected by radar altimetry: California,
741 Taiwan and north China. *Scientific Reports*, *6*, 28160. https://doi.org/10.1038/srep28160
742 Irons, J. R., Dwyer, J. L., & Barsi, J. A. (2012). The next Landsat satellite: The Landsat Data
743 Continuity Mission. *Remote Sensing of Environment*, *122*, 11–21.
744 https://doi.org/10.1016/j.rse.2011.08.026
745 Kanamitsu, M., Ebisuzaki, W., Woollen, J., Yang, S.-K., Hnilo, J. J., Fiorino, M., & Potter, G. L.
746 (2002). NCEP–DOE AMIP-II Reanalysis (R-2). *Bulletin of the American Meteorological*
747 *Society*, *83*(11), 1631–1644. https://doi.org/10.1175/BAMS-83-11-1631
748 Karegar, M.A., Dixon, T.H., Kusche, J., Chambers, D.P., 2018. A New Hybrid Method for Estimating
749 Hydrologically Induced Vertical Deformation From GRACE and a Hydrological Model: An
750 Example From Central North America. Journal of Advances in Modeling Earth Systems 10,
751 1196–1217. https://doi.org/10.1029/2017MS001181
752 Koirala, S., Yeh, P. J.-F., Hirabayashi, Y., Kanae, S., & Oki, T. (2013). Global-scale land surface
753 hydrologic modeling with the representation of water table dynamics. *Journal of Geophysical*
754 *Research: Atmospheres*, *119*(1), 75–89. https://doi.org/10.1002/2013JD020398
755 Kusche, J., Schmidt, R., Petrovic, S., & Rietbroek, R. (2009). Decorrelated GRACE time-variable
756 gravity solutions by GFZ, and their validation using a hydrological model. *Journal of*
757 *Geodesy*, *83*(10), 903–913. https://doi.org/10.1007/s00190-009-0308-3
758 Kustowski, B., Dziewoński, A.M., Ekström, G. (2007). Nonlinear crustal corrections for normal-mode
759 seismograms. *Bull. Seism. Soc. Am. 97(5)*, 1756 - 1762
760 Lemoine, J.-M., Bourgogne, S., Bruinsma, S., Gégout, P., Reinquin, F., & Biancale, R. (2015).
761 GRACE RL03-v2 monthly time series of solutions from CNES/GRGS (Vol. 17, p. 14461).

762 Presented at the EGU General Assembly Conference Abstracts. Available online at:
763 http://adsabs.harvard.edu/abs/2015EGUGA..1714461L
764 Lettenmaier, D. P., & Famiglietti, J. S. (2006). Hydrology: Water from on high. *Nature*, *444*(7119),
765 562. https://doi.org/10.1038/444562a
766 Longuevergne, L., Wilson, C., Scanlon, B. R., & Crétaux, J. F. (2013). GRACE water storage
767 estimates for the Middle East and other regions with significant reservoir and lake storage.
768 *Hydrology and Earth System Sciences, 17(12)*, 4817-4830.
769 Liu, Y.-C., Hwang, C., Han, J., Kao, R., Wu, C.-R., Shih, H.-C., & Tangdamrongsub, N. (2016).
770 Sediment-Mass Accumulation Rate and Variability in the East China Sea Detected by
771 GRACE. *Remote Sensing*, *8*(9), 777. https://doi.org/10.3390/rs8090777
772 Lu, X. X., & Siew, R. Y. (2006). Water discharge and sediment flux changes over the past decades in
773 the Lower Mekong River: possible impacts of the Chinese dams. *Hydrology and Earth*
774 *System Sciences*, *10*(2), 181–195. https://doi.org/10.5194/hess-10-181-2006
775 McFeeters, S. K. (1996). The use of the Normalized Difference Water Index (NDWI) in the
776 delineation of open water features. *International Journal of Remote Sensing*, *17*(7), 1425–
777 1432. https://doi.org/10.1080/01431169608948714
778 Mo, K. C., & Lettenmaier, D. P. (2013). Objective Drought Classification Using Multiple Land
779 Surface Models. *Journal of Hydrometeorology*, *15*(3), 990–1010.
780 https://doi.org/10.1175/JHM-D-13-071.1
781 Motagh, M., Walter, T.R., Sharifi, M.A., Fielding, E., Schenk, A., Anderssohn, J., Zschau, J., 2008.
782 Land subsidence in Iran caused by widespread water reservoir overexploitation. Geophysical
783 Research Letters 35. https://doi.org/10.1029/2008GL033814
784 Mu, D., Xu, T., Xu, G., 2019. Detecting coastal ocean mass variations with GRACE mascons.
785 Geophysical Journal International, 217, 2071–2080. https://doi.org/10.1093/gji/ggz138
786 Musa, Z. N., Popescu, I., & Mynett, A. (2015). A review of applications of satellite SAR, optical,
787 altimetry and DEM data for surface water modelling, mapping and parameter estimation.
788 *Hydrol. Earth Syst. Sci.*, *19*(9), 3755–3769. https://doi.org/10.5194/hess-19-3755-2015

789 Nahmani, S., Bock, O., Bouin, M.-N., Santamaría-Gómez, A., Boy, J.-P., Collilieux, X., et al. (2012).
790 Hydrological deformation induced by the West African Monsoon: Comparison of GPS,
791 GRACE and loading models. *Journal of Geophysical Research: Solid Earth*, *117*(B5),
792 B05409. https://doi.org/10.1029/2011JB009102
793 Nicholls, R.J., Cazenave, A., 2010. Sea-Level Rise and Its Impact on Coastal Zones. Science 328,
794 1517–1520. https://doi.org/10.1126/science.1185782
795 Niu, G. Y., Yang, Z. L., Dickinson, R. E., Gulden, L. E., & Su, H. (2007). Development of a simple
796 groundwater model for use in climate models and evaluation with Gravity Recovery and
797 Climate Experiment data. Journal of Geophysical Research: Atmospheres, 112(D7).
798 O'Grady, D., Leblanc, M., & Gillieson, D. (2011). Use of ENVISAT ASAR Global Monitoring Mode
799 to complement optical data in the mapping of rapid broad-scale flooding in Pakistan.
800 *Hydrology and Earth System Sciences*, *15*(11), 3475–3494. https://doi.org/10.5194/hess-15-
801 3475-2011
802 Oh, T. H., Pang, S. Y., & Chua, S. C. (2010). Energy policy and alternative energy in Malaysia:
803 Issues and challenges for sustainable growth. *Renewable and Sustainable Energy Reviews*,
804 *14*(4), 1241–1252. https://doi.org/10.1016/j.rser.2009.12.003
805 Othman, A., Sultan, M., Becker, R., Alsefry, S., Alharbi, T., Gebremichael, E., Alharbi, H.,
806 Abdelmohsen, K., 2018. Use of Geophysical and Remote Sensing Data for Assessment of
807 Aquifer Depletion and Related Land Deformation. Surv Geophys 39, 543–566.
808 https://doi.org/10.1007/s10712-017-9458-7
809 Rabus, B., Eineder, M., Roth, A., Bamler, R. (2003). The shuttle radar topography mission—a new
810 class of digital elevation models acquired by spaceborne radar. ISPRS Journal of
811 Photogrammetry and Remote Sensing 57, 241–262. https://doi.org/10.1016/S0924-
812 2716(02)00124-7
813 Rodell, M., Houser, P. R., Jambor, U., Gottschalck, J., Mitchell, K., Meng, C.-J., et al. (2004). The
814 Global Land Data Assimilation System. *Bulletin of the American Meteorological Society*,
815 *85*(3), 381–394. https://doi.org/10.1175/BAMS-85-3-381

816 Roebber, P. J. (2009). Visualizing Multiple Measures of Forecast Quality. *Weather and Forecasting*,
817 *24*(2), 601–608. https://doi.org/10.1175/2008WAF2222159.1
818 Sakumura, C., Bettadpur, S., & Bruinsma, S. (2014). Ensemble prediction and intercomparison
819 analysis of GRACE time-variable gravity field models. *Geophysical Research Letter*, 41,
820 1389–1397. doi:10.1002/2013GL058632
821 Santamaría-Gómez, A., Gravelle, M., Dangendorf, S., Marcos, M., Spada, G., & Wöppelmann, G.
822 (2017). Uncertainty of the 20th century sea-level rise due to vertical land motion errors. *Earth*
823 *and Planetary Science Letters*, *473*, 24–32. https://doi.org/10.1016/j.epsl.2017.05.038
824 Shirleym R., & Kammen, D. (2015). Energy planning and development in Malaysian Borneo:
825 Assessing the benefits of distributed technologies versus large scale energy mega-projects.
826 *Energy Strategy Reviews*, 8, 15 – 29. http://dx.doi.org/10.1016/j.esr.2015.07.001.
827 Simon, K. M., Riva, R. E. M., Kleinherenbrink, M., & Tangdamrongsub, N. (2017). A data-driven
828 model for constraint of present-day glacial isostatic adjustment in North America. *Earth and*
829 *Planetary Science Letters*, *474*, 322–333. https://doi.org/10.1016/j.epsl.2017.06.046
830 Sovacool, B. K., & Bulan, L. C. (2011). Behind an ambitious megaproject in Asia: The history and
831 implications of the Bakun hydroelectric dam in Borneo. *Energy Policy*, *39*(9), 4842–4859.
832 https://doi.org/10.1016/j.enpol.2011.06.035
833 Steckler, M.S., Nooner, S.L., Akhter, S.H., Chowdhury, S.K., Bettadpur, S., Seeber, L., Kogan, M.G.,
834 2010. Modeling Earth deformation from monsoonal flooding in Bangladesh using
835 hydrographic, GPS, and Gravity Recovery and Climate Experiment (GRACE) data. Journal
836 of Geophysical Research: Solid Earth 115. https://doi.org/10.1029/2009JB007018
837 Swenson, S., Chambers, D., & Wahr, J. (2008). Estimating geocenter variations from a combination
838 of GRACE and ocean model output. *Journal of Geophysical Research: Solid Earth*, *113*(B8),
839 B08410. https://doi.org/10.1029/2007JB005338
840 Syed, T. H., Famiglietti, J. S., Rodell, M., Chen, J., & Wilson, C. R. (2008). Analysis of terrestrial
841 water storage changes from GRACE and GLDAS. *Water Resources Research*, *44*(2).
842 https://doi.org/10.1029/2006WR005779

Tachikawa, T., Hato, M., Kaku, M., Iwasaki, A. (2011). Characteristics of ASTER GDEM version 2, in: 2011 IEEE International Geoscience and Remote Sensing Symposium. Presented at the 2011 IEEE International Geoscience and Remote Sensing Symposium, pp. 3657–3660. https://doi.org/10.1109/IGARSS.2011.6050017

Tadono, T., Takaku, J., Tsutsui, K., Oda, F., Nagai, H. (2015). Status of ALOS World 3D (AW3D) Global DSM Generation. In: 2015 IEEE International Geoscience and Remote Sensing Symposium (IGARSS), pp. 3822–3825 July

Tangdamrongsub, N., Han, S.-C., Decker, M., Yeo, I.-Y., & Kim, H. (2018). On the use of the GRACE normal equation of inter-satellite tracking data for estimation of soil moisture and groundwater in Australia. *Hydrology and Earth System Sciences*, *22*(3), 1811–1829. https://doi.org/10.5194/hess-22-1811-2018

Tangdamrongsub, N., Steele-Dunne, S.C., Gunter, B.C., Ditmar, P.G., Sutanudjaja, E.H., Sun, Y., Xia, T., Wang, Z., 2017. Improving estimates of water resources in a semi-arid region by assimilating GRACE data into the PCR-GLOBWB hydrological model. Hydrology and Earth System Sciences 21, 2053–2074. https://doi.org/https://doi.org/10.5194/hess-21-2053-2017

Tapley, B. D., Bettadpur, S., Ries, J. C., Thompson, P. F., & Watkins, M. M. (2004). GRACE Measurements of Mass Variability in the Earth System. *Science*, *305*(5683), 503–505. https://doi.org/10.1126/science.1099192

Tatsumi, K., & Yamashiki, Y. (2015). Effect of irrigation water withdrawals on water and energy balance in the Mekong River Basin using an improved VIC land surface model with fewer calibration parameters. *Agricultural Water Management*, *159*, 92–106. https://doi.org/10.1016/j.agwat.2015.05.011

Tourian, M.J., Elmi, O., Chen, Q., Devaraju, B., Roohi, S., Sneeuw, N., 2015. A spaceborne multisensor approach to monitor the desiccation of Lake Urmia in Iran. Remote Sensing of Environment 156, 349–360. https://doi.org/10.1016/j.rse.2014.10.006

Tiwari, V.M., Srinivas, N., Singh, B., 2014. Hydrological changes and vertical crustal deformation in south India: Inference from GRACE, GPS and absolute gravity data. Physics of the Earth and Planetary Interiors 231, 74–80. https://doi.org/10.1016/j.pepi.2014.03.002

Tscherning, C. C., & Rapp, R. H. (1974). Closed covariance expressions for gravity anomalies, geoid undulations, and deflections of the vertical implied by anomaly degree variance models. Report of the Department of Geodetic Science No. 208, pp. 89, The Ohio State University

van Dam, T., Wahr J., & Lavallée David. (2007). A comparison of annual vertical crustal displacements from GPS and Gravity Recovery and Climate Experiment (GRACE) over Europe. *Journal of Geophysical Research: Solid Earth*, *112*(B3). https://doi.org/10.1029/2006JB004335

Vergnes, J. P., & Decharme, B. (2012). A simple groundwater scheme in the TRIP river routing model: global off-line evaluation against GRACE terrestrial water storage estimates and observed river discharges. Hydrology and Earth System Sciences, 16(10), 3889-3908.

Wahr, J., Molenaar, M., & Bryan, F. (1998). Time variability of the Earth's gravity field: Hydrological and oceanic effects and their possible detection using GRACE. *Journal of Geophysical Research: Solid Earth*, *103*(B12), 30205–30229. https://doi.org/10.1029/98JB02844

Wahr, J., Khan, S. A., van Dam, T., Liu, L., van Angelen, J. H., van den Broeke, M. R., & Meertens, C. M. (2013). The use of GPS horizontals for loading studies, with applications to northern California and southeast Greenland. *Journal of Geophysical Research: Solid Earth*, *118*(4), 1795–1806. https://doi.org/10.1002/jgrb.50104

Wang, B., Wu, R., & Fu, X. (2000). Pacific–East Asian Teleconnection: How Does ENSO Affect East Asian Climate? *Journal of Climate*, *13*(9), 1517–1536. https://doi.org/10.1175/1520-0442(2000)013<1517:PEATHD>2.0.CO;2

Wang, H., Xiang, L., Jia, L., Jiang, L., Wang, Z., Hu, B., Gao, P. (2012). Load Love numbers and Green's functions for elastic Earth models PREM, iasp91, ak135, and modified models with refined crustal structure from Crust 2.0. *Computers & Geosciences*, *49*, 190 – 199. http://dx.doi.org/10.1016/j.cageo.2012.06.022

Wang, L., Chen, C., Du, J., & Wang, T. (2017). Detecting seasonal and long-term vertical displacement in the North China Plain using GRACE and GPS. *Hydrology and Earth System Sciences*, *21*(6), 2905–2922. https://doi.org/10.5194/hess-21-2905-2017

Wang, X., de Linage, C., Famiglietti, J., & Zender, C. S. (2011). Gravity Recovery and Climate Experiment (GRACE) detection of water storage changes in the Three Gorges Reservoir of China and comparison with in situ measurements. *Water Resources Research*, *47*(12), W12502. https://doi.org/10.1029/2011WR010534

Watkins, M. M., & Yuan, D. N. (2014). GRACE JPL level-2 processing standards document for level-2 product release 05.1. Jet Propulsion Laboratory, California.

Wu, H., Adler, R. F., Tian, Y., Huffman, G. J., Li, H., & Wang, J. (2014). Real-time global flood estimation using satellite-based precipitation and a coupled land surface and routing model. *Water Resources Research*, *50*(3), 2693–2717. https://doi.org/10.1002/2013WR014710

Yang, Z. L., Niu, G. Y., Mitchell, K. E., Chen, F., Ek, M. B., Barlage, M., ... & Xia, Y. (2011). The community Noah land surface model with multiparameterization options (Noah- MP): 2. Evaluation over global river basins. Journal of Geophysical Research: Atmospheres, 116(D12).

Yi, S., Song, C., Wang, Q., Wang, L., Heki, K., Sun, W., 2017. The potential of GRACE gravimetry to detect the heavy rainfall-induced impoundment of a small reservoir in the upper Yellow River. Water Resources Research 53, 6562–6578. https://doi.org/10.1002/2017WR020793

Zerbin, S., Richter, B., Rocca, F., van Dam, T., & Matonti, F. (2007). A Combination of Space and Terrestrial Geodetic Techniques to Monitor Land Subsidence: Case Study, the Southeastern Po Plain, Italy. *Journal of Geophysical Research: Solid Earth*, *112*(B5). https://doi.org/10.1029/2006JB004338

Zhou, H., Luo, Z., Tangdamrongsub, N., Zhou, Z., He, L., Xu, C., Li, Q., Wu, Y., 2018. Identifying Flood Events over the Poyang Lake Basin Using Multiple Satellite Remote Sensing Observations, Hydrological Models and In Situ Data. Remote Sensing 10, 713. https://doi.org/10.3390/rs10050713

924 **List of figure captions**

925 Fig. 1. (a) The overall geographical location of the study area and the location of the GPS station
926 BIN1. The white rectangle identifies the location of Bakun Dam and Bakun Lake. The background
927 presents the elevation. (b) Zoom-in locations of the Bakun Dam and Bakun Lake. (c) The Landsat's
928 natural color image of the Bakun Lake on August 12, 2010 (prior to filling). (d) The Landsat image of
929 the Bakun Lake on August 4, 2013 (after the dam is online).

930 Fig. 2. Data processing diagram of this study. The section number (Sect) indicates the location where
931 the explanation can be found.

932 Fig. 3. The yearly average NDWI (a – j) and the yearly estimated area (k) of the Bakun Lake derived
933 from Landsat data between 2007 and 2016.

934 Fig. 4. (a) The Bakun Lake's water pixel estimated based on the Landsat-derived NDWI between
935 2012 and 2016 (post-dam period). (b – d) The simulated flood extension using a different averaged
936 water level, approximately 46 m, 60 m, and 73 m, respectively.

937 Fig. 5. The critical success index (CSI) associated with the different DEMs and averaged water level.

938 Fig. 6. The mean value (solid) and the standard deviation (envelop) of GRACE-derived monthly
939 ΔTWS (in millimeter, left axis) over the Bakun Lake between August 2002 and March 2016. The time
940 series associated with the right axis is the approximated Lake level (in meters) derived from the TWS
941 forward model. The vertical dotted lines between August 2010 and December 2011 denote the
942 impounding period.

943 Fig. 7. (a) The ΔTWS difference between the post- and pre-dam period. Warm colors indicate
944 increased water. (b) Normalized empirical covariance function derived from GRACE solutions (CSR,
945 JPL, GFZ, GRGS, and average) between 2003 and 2016. (c) The increased ΔTWS simulated from the
946 TWS forward model. (d) The variance ratio associated with the different simulated water level.

947 Fig. 8. (a) The simulated ΔTWS over the Bakun Lake from four different LSM products (CABLE,
948 GLDAS, NCEP, ECMWF) between August 2002 and March 2016 (see legends in (b)). The vertical

dotted lines between August 2010 and December 2011 denote the impounding period. (b) The model-associated yearly precipitation over the Bakun Lake. (c – f) The LSMs-simulated ΔTWS difference between the post- and pre-dam period. (g – j) The model-associated precipitation difference between the post- and pre-dam period.

Fig. 9. (a) The vertical displacement computed using the disk load model. The placement (location) of the disk loads is shown in the insert figure (zoom in of the white-dash boundary). (b) The vertical displacement computed using the GRACE SHC data. Note that (a) and (b) use different color scales.

Fig. 10. The vertical displacement induced by the placement of two different disk loads with the same mass (0.7 Gton) but different shape, Disk 1 (radius = 150 km, thickness = 1 cm, black), and Disk 2 (radius = 15 km, thickness = 1 m, blue) on the Earth's surface. For a visualization purpose, the symbols of Disk 1 and Disk 2 are not scaled. The vertical displacement is computed to different maximum harmonic degrees (N_{max} = 90 (dash), and 40,000 (solid)). The insert figure is the zoom-in of the result around the disk's center.

Fig. 11. The vertical displacement computed using the disk load model associated with (a) various disk thickness derived from lake filling model, and (b) uniform (average) disk thickness. The location of BIN1 station and the Bakun Dam is displayed as points A (green) and B (red). (c) The cross-section profile of vertical displacement between points A and B obtained from (a) and (b).

Fig. 12. The cross-section of vertical displacement between points A and B (Fig. 9), derived from different sets of Load Love Numbers. The insert figure is the zoom-in of the dashed rectangle.

Fig. 13. The vertical displacement at BIN1 station computed using (a) the disk load model, GRACE SHC data, and (b) GPS observations (UNR, ULR). The vertical dotted lines between August 2010 and December 2011 denote the impounding period. The thick solid lines are the estimated trend during the impoundment, and the dashed lines are the trend during pre- and post-dam period. The envelop represents the error of the displacement estimate.

973 Fig. 14. Scatter plots of the vertical deformation between (a) GPS-UNR and GPS-ULR, (b) GPS-UNR
974 and GRACE SHC, and (c) GPS-UNR and disk load model. The correlation coefficient (ρ) associated
975 to each scatter plot is also given.

976 Fig. 15. The horizontal displacement ((a, c) East, (b, d) North) at BIN1 station computed using the
977 disk load model, GRACE SHC data, and GPS observations (UNR, ULR). The vertical dotted lines
978 between August 2010 and December 2011 denotes the impounding period. The thick solid lines are
979 the estimated (fitted) trend during the impoundment, and the envelop represents the error of the
980 displacement estimate.

981 Fig. 16. The horizontal displacement ((a) East, (b) North) at BIN1 station computed using the disk
982 load model, GRACE SHC data, and GPS observations (UNR, ULR). The vertical dotted lines
983 between August 2010 and December 2011 denotes the impounding period. The thick solid lines are
984 the estimated (fitted) trend during the impounding period.

985

986 **Table 1** Summary of satellite remote sensing applications related to TWS change of land subsidence

Loading sources	Regions	Datasets	Findings	References
Seasonal snow	Japan	GPS	Heavy snow build up contributes to annual surface displacement.	Heki (2001)
Monsoonal flooding	Bangladesh	GRACE, GPS	Flood water of 100-150 Gt influences a vertical deformation up to 6 cm.	Steckler et al. (2010)
Mountain snow and ice	Nepal Himalaya	GRACE, GPS	Detection of surface uplift causes by melting ice and snow.	Fu and Freymueller (2012)
Rainfall	Amazon, Southeast Asia	GRACE, GPS	Heavy precipitation induces oscillation in the GPS horizontal components.	Bettinelli et al. (2008); Fu et al. (2013)
	India	GRACE, GPS, absolute gravity data	Hydrological effects are the major cause of periodic surface deformation.	Tiwari et al. (2014)
Groundwater depletion	Central Mexico	SAR, InSAR	Groundwater overexploitation causes significant land subsidence over the regions.	Castellazzi et al. (2016)
	North China Plain,	GRACE, GPS		Wang et al. (2017)
	Iran	InSAR, Landsat		Motagh et al. (2008)
	Saudi Arabia	GRACE, SAR, Landsat, GPS		Othman et al. (2017)
	California, Taiwan, North China	GRACE, altimetry, GPS		Hwang et al. (2016)
Reservoir impoundment	Malaysia	GRACE, Landsat, GPS	Impoundment period of the reservoir induces a large extent land subsidence.	This study

987

988

989 **Table 2** Trend, annual amplitude, and phase (calendar month) estimate computed from the GRACE-
990 derived ΔTWS and four different LSM-simulated ΔTWS in the pre- and post-dam periods.

	Pre-dam			Post-dam		
	trend (mm/year)	amplitude (mm)	phase (month)	trend (mm/year)	amplitude (mm)	phase (month)
GRACE	2.9 ± 1.0	16.1 ± 6.4	Dec	2.3 ± 4.2	38.2 ± 14.7	Feb
CABLE	3.2 ± 0.8	34.5 ± 5.4	Feb	-8.2 ± 2.0	48.4 ± 6.9	Jan
GLDAS	3.9 ± 0.4	19.7 ± 2.5	Jan	-9.1 ± 1.5	34.4 ± 5.3	Feb
NCEP	16.0 ± 0.8	19.9 ± 5.6	Feb	-2.5 ± 1.2	11.5 ± 4.1	Jan
ECMWF	15.4 ± 1.0	42.1 ± 6.8	Feb	-1.5 ± 1.4	35.0 ± 5.0	Jan

991

992 **Table 3** The cross-correlation values (with 0.05 significant level) between GRACE and four different
993 LSMs. The seasonal variation is removed (based on Least-squares fit, see Appendix A) before
994 computing the correlation.

	GRACE	CABLE	GLDAS	NCEP	ECMWF
GRACE	1.00				
CABLE	-0.29	1.00			
GLDAS	-0.21	0.73	1.00		
NCEP	0.20	0.22	0.29	1.00	
ECMWF	0.18	0.23	0.32	0.84	1.00

995

996

997 **Table 4** Total change of the 3D displacement (mm) between August 2010 and December 2011
998 estimated using the disk load model, GRACE SHC data, and GPS observations (UNR, ULR).

	Up	North	East
Disk load model	-8.77 ± 0.08	-2.35 ± 0.02	3.32 ± 0.03
GRACE	-1.76 ± 0.06	0.04 ± 0.02	0.48 ± 0.02
UNR	-9.52 ± 0.23	-3.28 ± 0.11	-1.72 ± 0.13
ULR	-10.52 ± 0.26	-1.60 ± 0.12	2.47 ± 0.14

999

1000

1001 **Table 5** Strength and limitation of different remote sensing data and numerical models found from

1002 this study

Observation, model	Strength	Limitation
GRACE	Provide total water storage, including surface and underground water components. Concentrate mass over a small area is recoverable.	Spatial and temporal limited to a few hundred km and one month. Only provide the integrated water column, and cannot be disaggregated.
Landsat	Capture high spatial resolution surface reflectance, which can be effectively used to delineate the surface water area.	Only provide surface water component. Limited number of "cloud free" scenes.
GPS	Frequently observe the surface deformation at the local scale.	Like GRACE, GPS senses an integrated deformation. Intensive care of data gaps, outliers, and noises are required.
LSM	Simulate the individual hydrological component separately at any spatial and temporal scale.	The uncertainty is generally high due to the imperfect representation of model physics (e.g., lack of manmade reservoir component).
Forward model	Simulate possible hydrological and geophysical signals based on the empirical relationship between the designed model and observation. The method is easy to implement.	Similar to LSM, the accuracy highly depends on the knowledge used to construct the model and the quality of the observation.
Disk load model	Utilize the strength of GRACE and Landsat data to estimate the local land deformation.	

1003

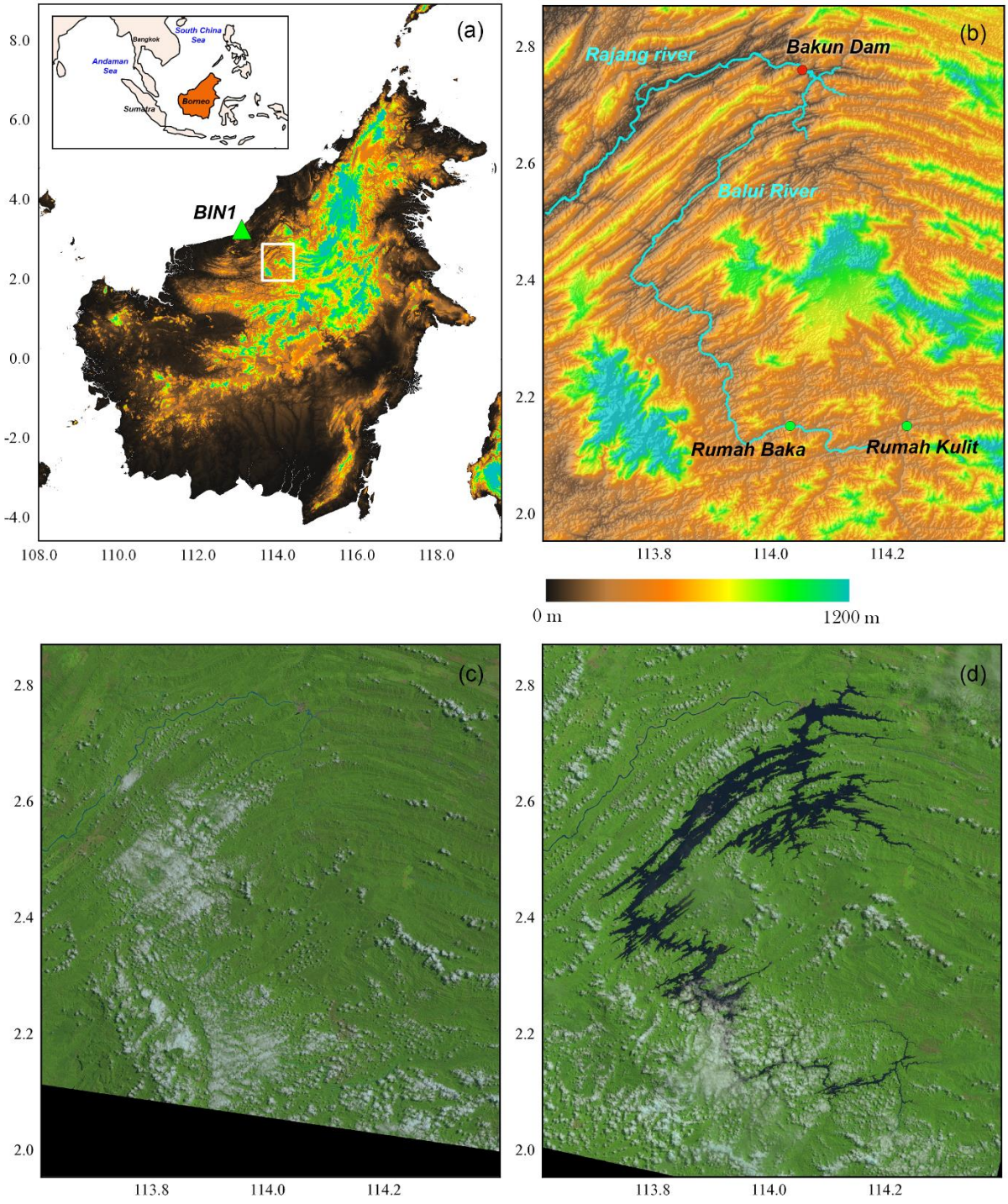

1004

1005 **Fig. 1**. (a) The overall geographical location of the study area and the location of the GPS station
1006 BIN1. The white rectangle identifies the location of Bakun Dam and Bakun Lake. The background
1007 presents the elevation. (b) Zoom-in locations of the Bakun Dam and Bakun Lake. (c) The Landsat's
1008 natural color image of the Bakun Lake on August 12, 2010 (prior to filling). (d) The Landsat image of
1009 the Bakun Lake on August 4, 2013 (after the dam is online).

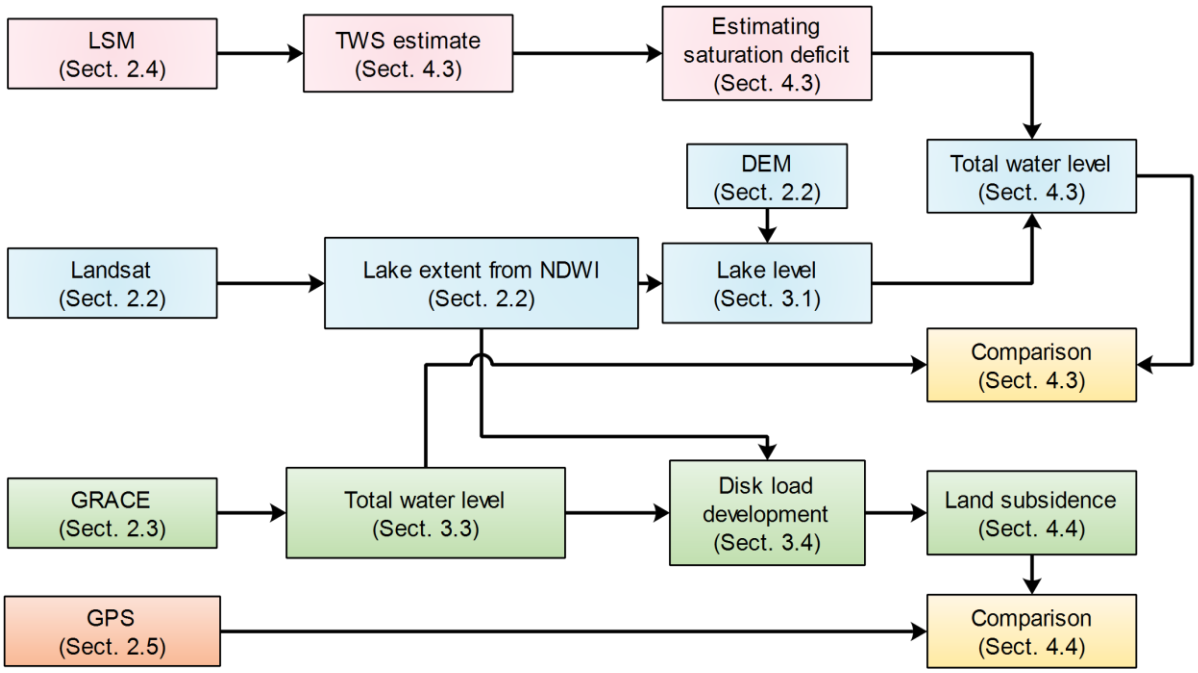

Fig. 2. Data processing diagram of this study. The section number (Sect) indicates the location where the explanation can be found.

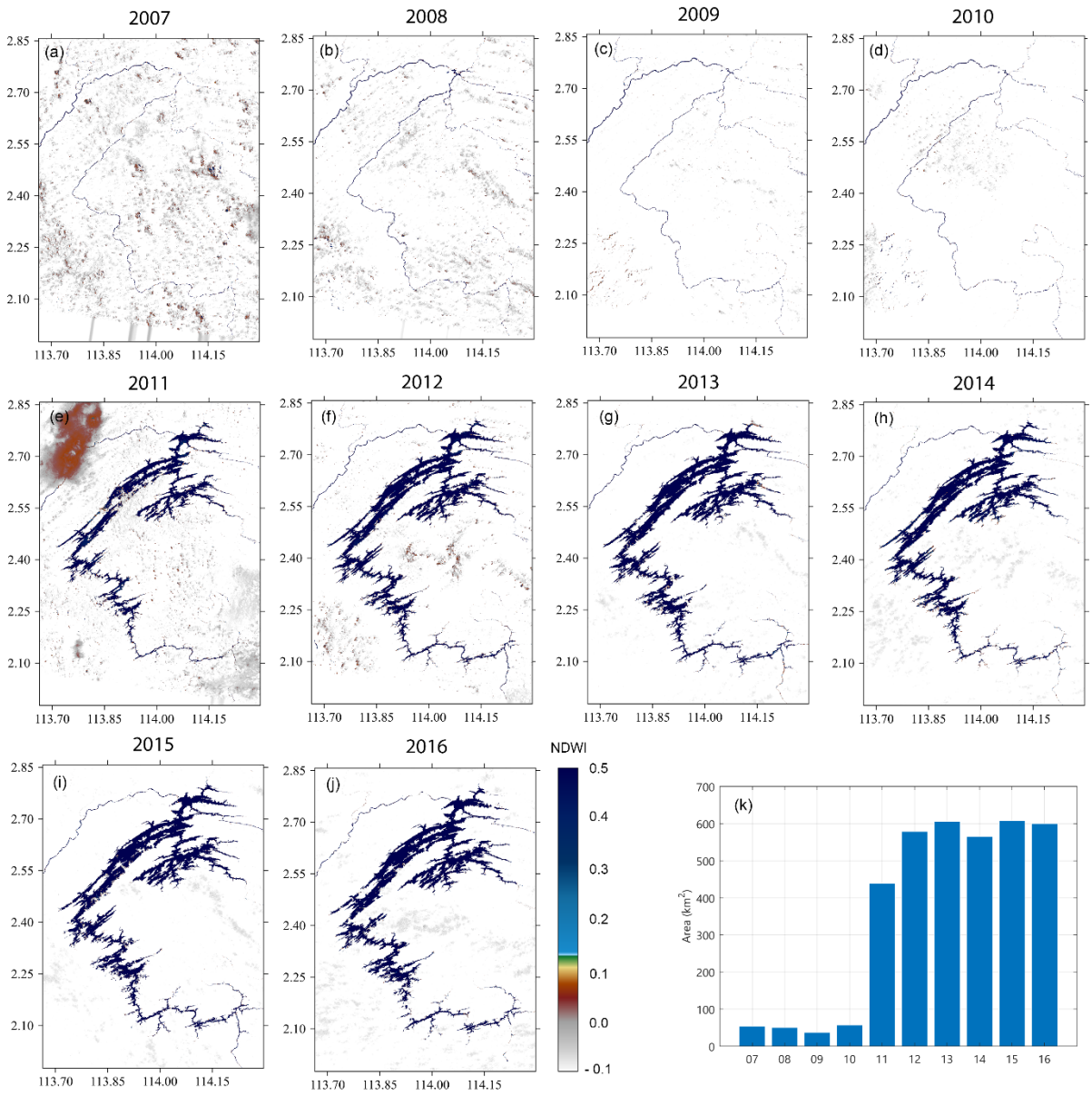

Fig. 3. The yearly average NDWI (a – j) and the yearly estimated area (k) of the Bakun Lake derived from Landsat data between 2007 and 2016.

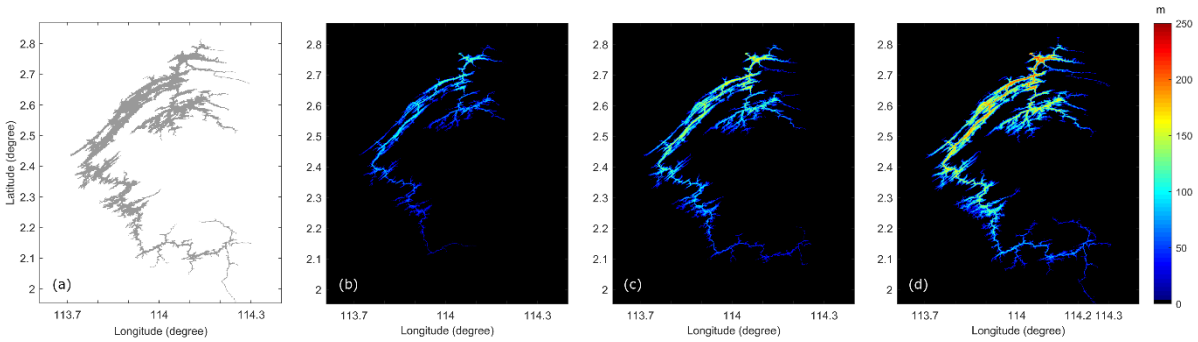

1018

1019 **Fig. 4.** (a) The Bakun Lake's water pixel estimated based on the Landsat-derived NDWI between

1020 2012 and 2016 (post-dam period). (b – d) The simulated flood extension using a different averaged

1021 water level, approximately 46 m, 60 m, and 73 m, respectively.

1022

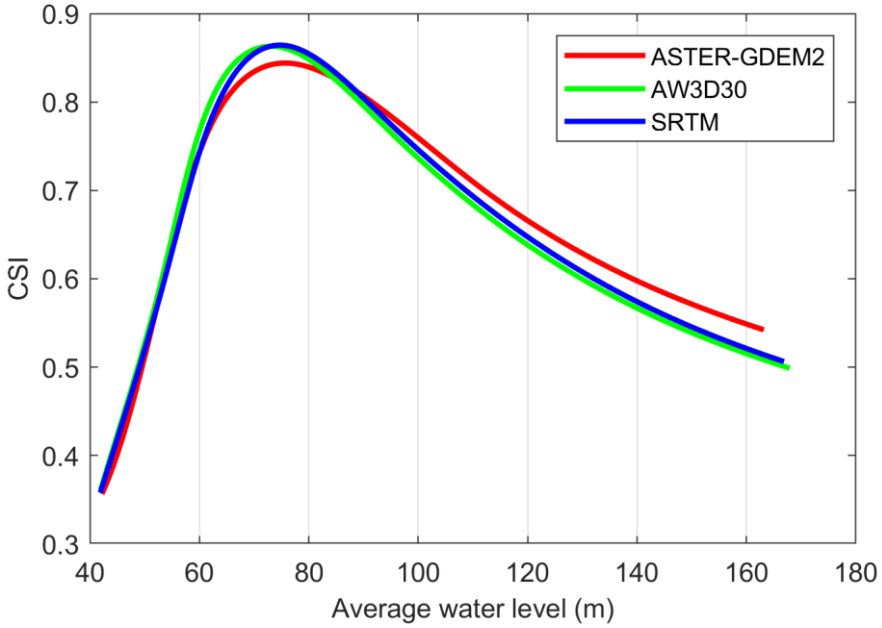

1023

1024 **Fig. 5.** The critical success index (CSI) associated with the different DEMs and averaged water level.

1025

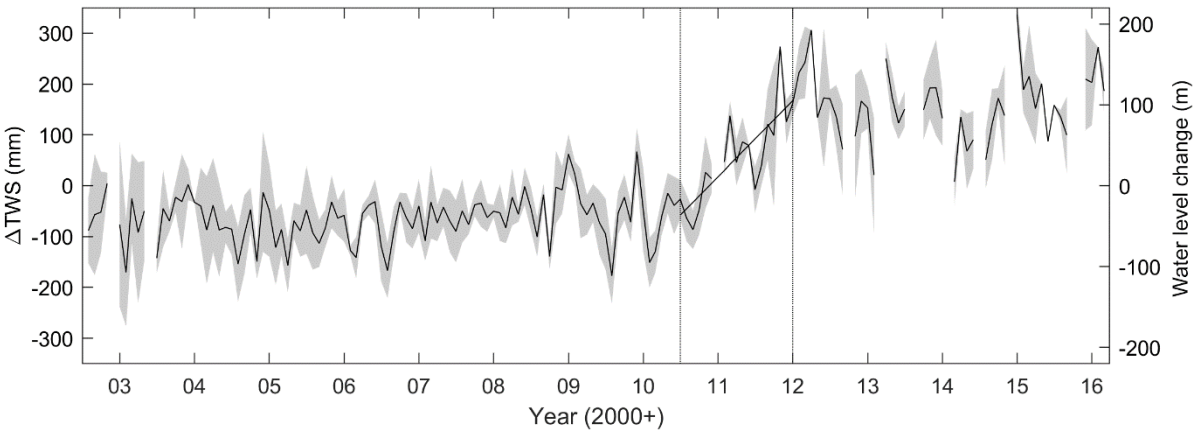

Fig. 6. The mean value (solid) and the standard deviation (envelop) of GRACE-derived monthly ΔTWS (in millimeter, left axis) over the Bakun Lake between August 2002 and March 2016. The time series associated with the right axis is the approximated Lake level (in meters) derived from the TWS forward model. The vertical dotted lines between August 2010 and December 2011 denote the impounding period.

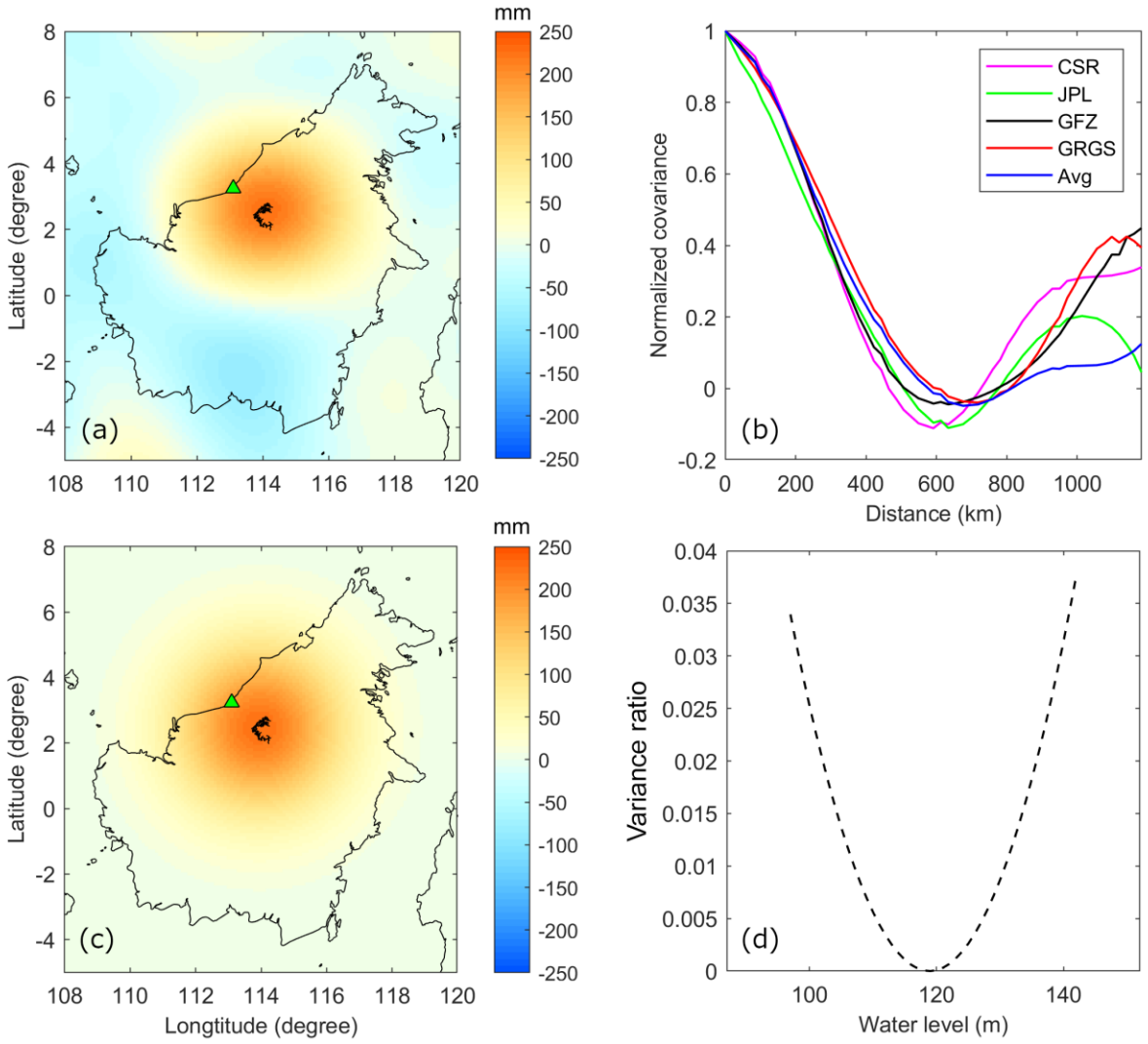

1033

1034 **Fig. 7.** (a) The ΔTWS difference between the post- and pre-dam period. Warm colors indicate

1035 increased water. (b) Normalized empirical covariance function derived from GRACE solutions (CSR,

1036 JPL, GFZ, GRGS, and average) between 2003 and 2016. (c) The increased ΔTWS simulated from the

1037 TWS forward model. (d) The variance ratio associated with the different simulated water level.

1038

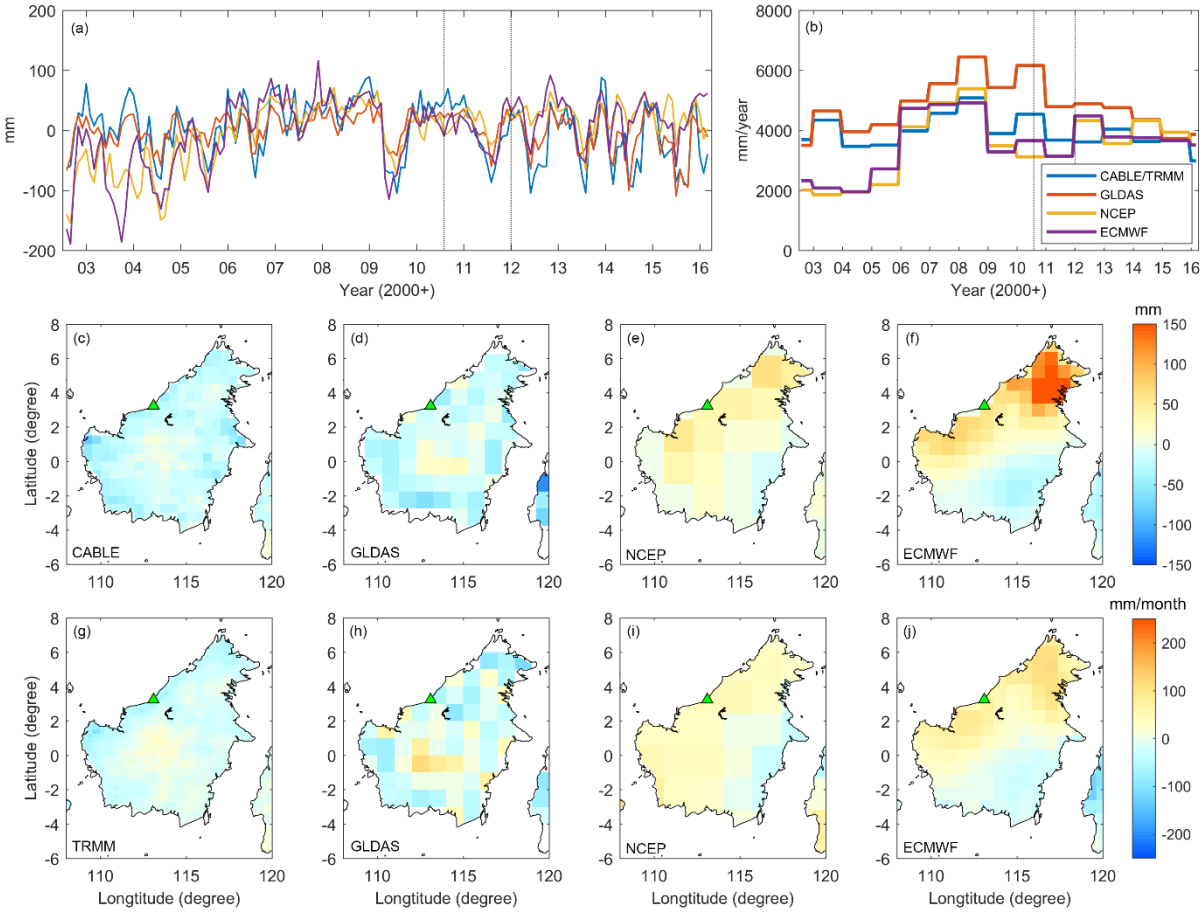

1039

1040 **Fig. 8**. (a) The simulated ΔTWS over the Bakun Lake from four different LSM products (CABLE,
1041 GLDAS, NCEP, ECMWF) between August 2002 and March 2016 (see legends in (b)). The vertical
1042 dotted lines between August 2010 and December 2011 denote the impounding period. (b) The model-
1043 associated yearly precipitation over the Bakun Lake. (c – f) The LSMs-simulated ΔTWS difference
1044 between the post- and pre-dam period. (g – j) The model-associated precipitation difference between
1045 the post- and pre-dam period.

1046

1047

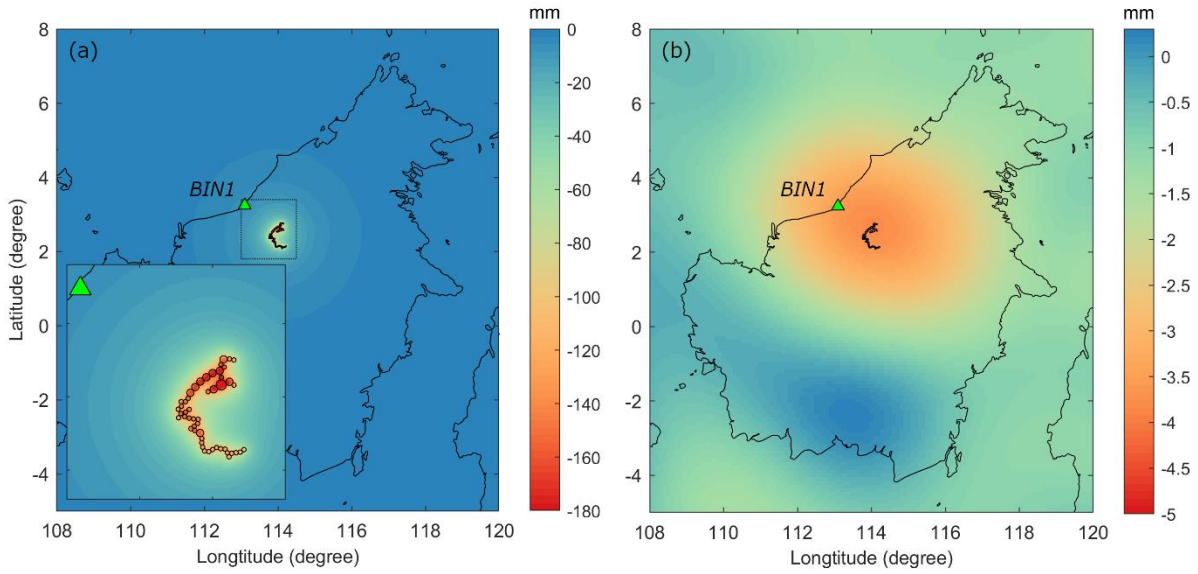

1048

1049 **Fig. 9.** (a) The vertical displacement computed using the disk load model. The placement (location) of

1050 the disk loads is shown in the insert figure (zoom in of the white-dash boundary). (b) The vertical

1051 displacement computed using the GRACE SHC data. Note that (a) and (b) use different color scales.

1052

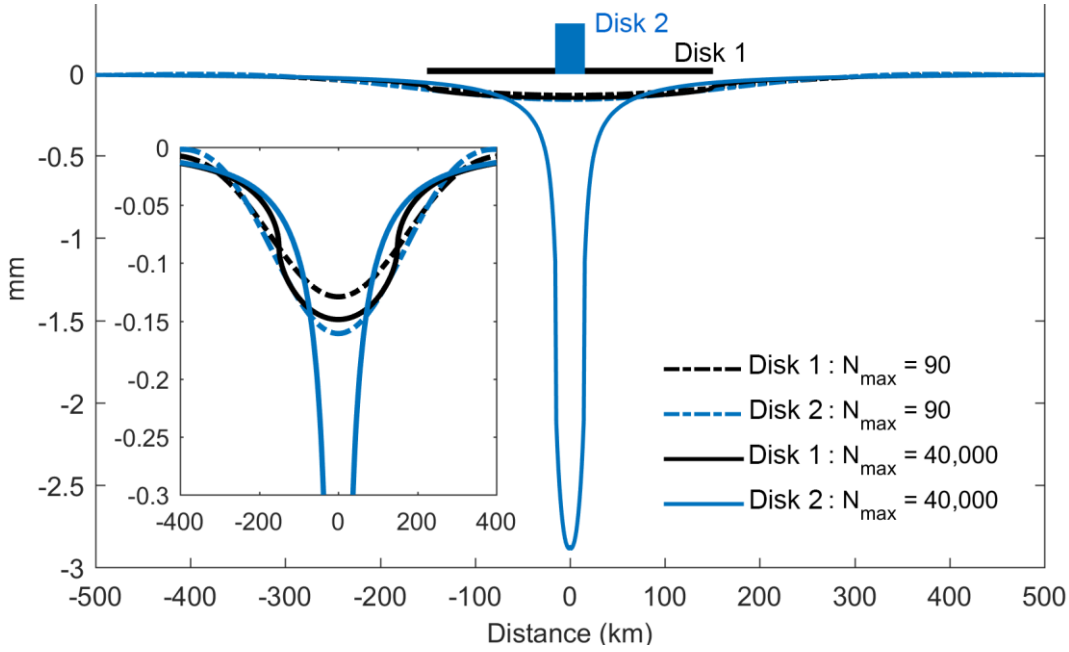

1053

1054 **Fig. 10**. The vertical displacement induced by the placement of two different disk loads with the same
1055 mass (0.7 Gton) but different shape, Disk 1 (radius = 150 km, thickness = 1 cm, black), and Disk 2
1056 (radius = 15 km, thickness = 1 m, blue) on the Earth's surface. For a visualization purpose, the
1057 symbols of Disk 1 and Disk 2 are not scaled. The vertical displacement is computed to different
1058 maximum harmonic degrees (N_{max} = 90 (dash), and 40,000 (solid)). The insert figure is the zoom-in of
1059 the result around the disk's center.

1060

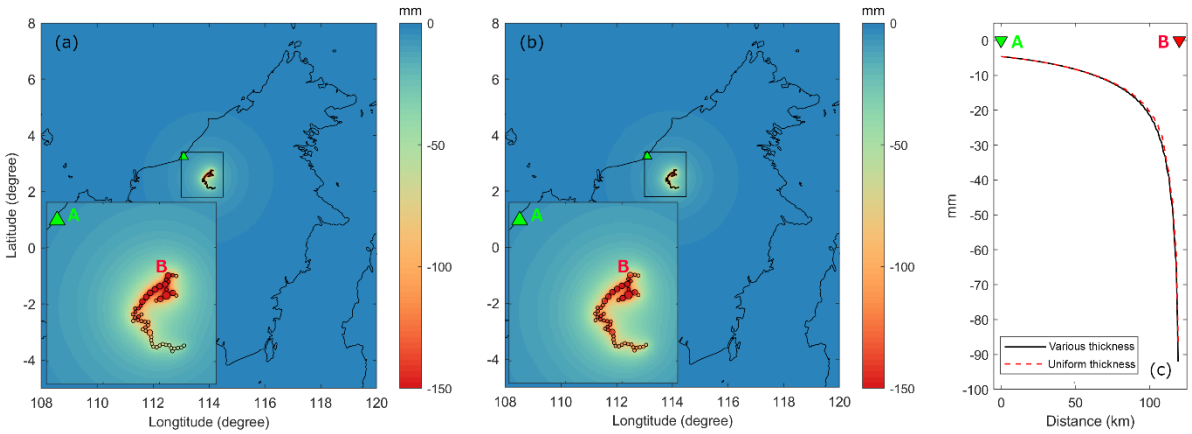

1061

1062 **Fig. 11.** The vertical displacement computed using the disk load model associated with (a) various
1063 disk thickness derived from lake filling model, and (b) uniform (average) disk thickness. The location
1064 of BIN1 station and the Bakun Dam is displayed as points A (green) and B (red). (c) The cross-section
1065 profile of vertical displacement between points A and B obtained from (a) and (b).

1066

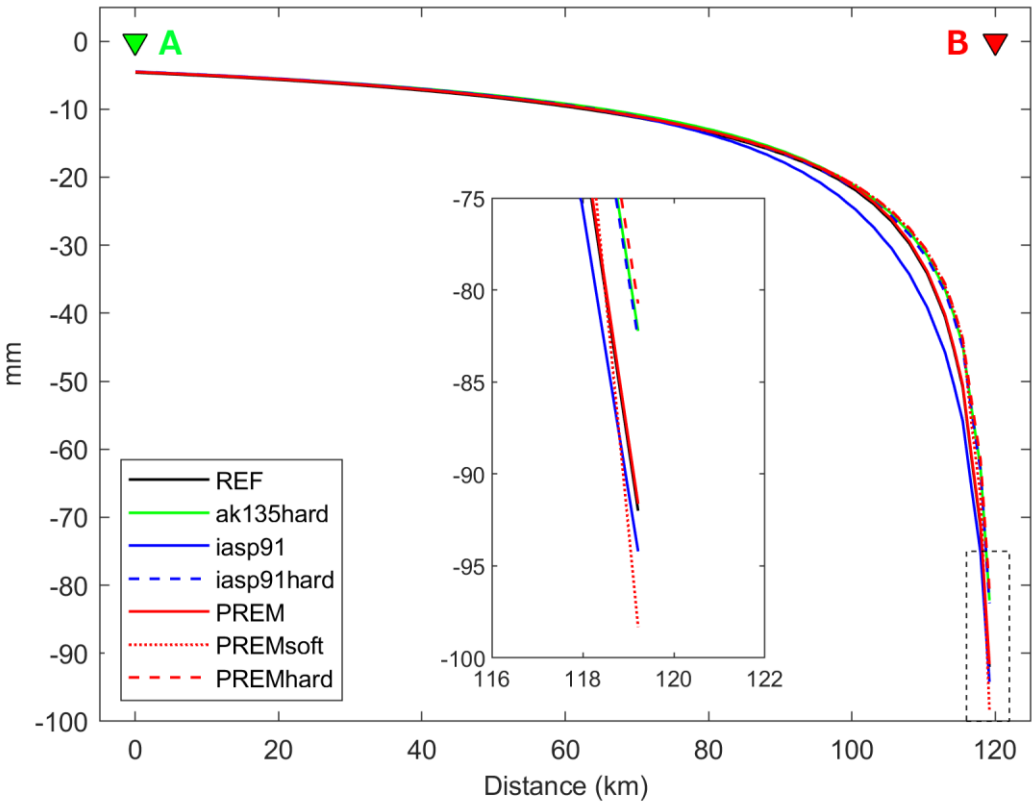

1067

1068 **Fig. 12.** The cross-section of vertical displacement between points A and B (Fig. 9), derived from

1069 different sets of Load Love Numbers. The insert figure is the zoom-in of the dashed rectangle.

1070

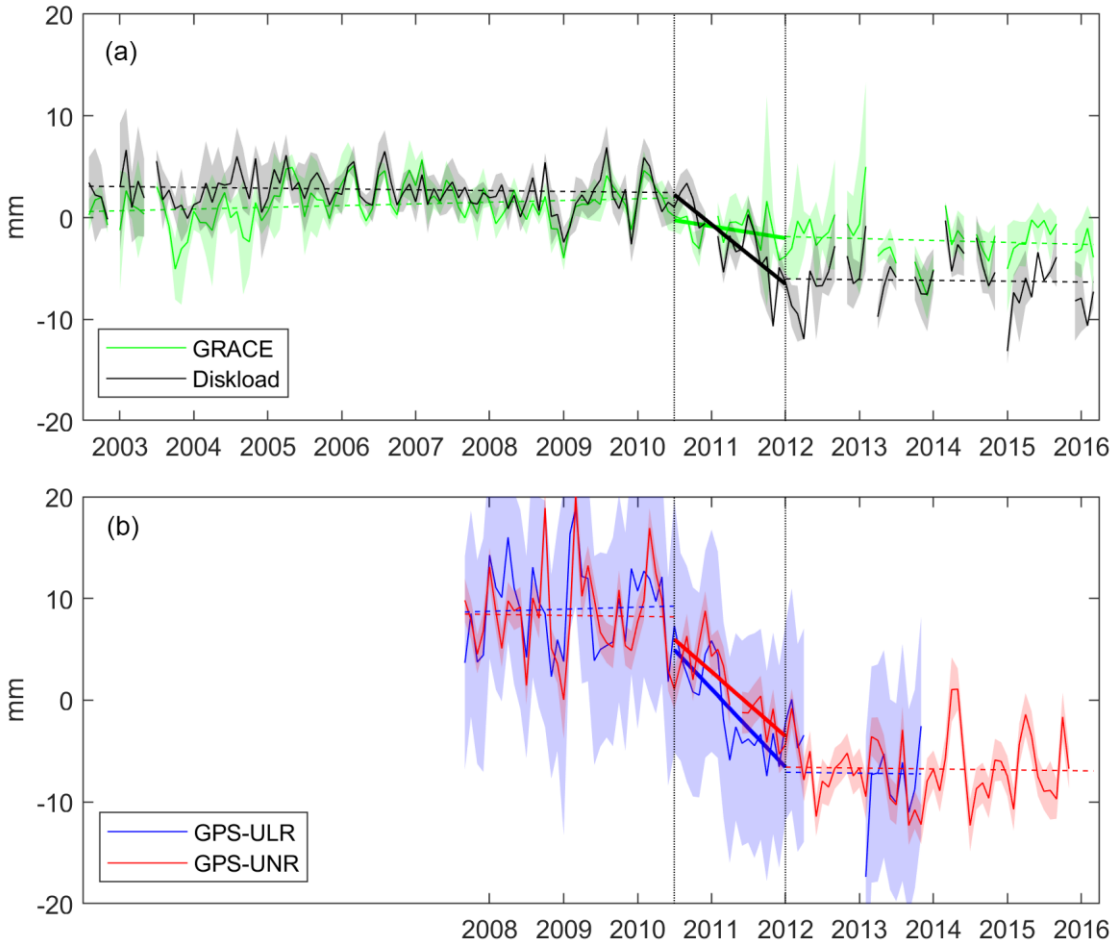

Fig. 13. The vertical displacement at BIN1 station computed using (a) the disk load model, GRACE SHC data, and (b) GPS observations (UNR, ULR). The vertical dotted lines between August 2010 and December 2011 denote the impounding period. The thick solid lines are the estimated trend during the impoundment, and the dashed lines are the trend during pre- and post-dam period. The envelop represents the error of the displacement estimate.

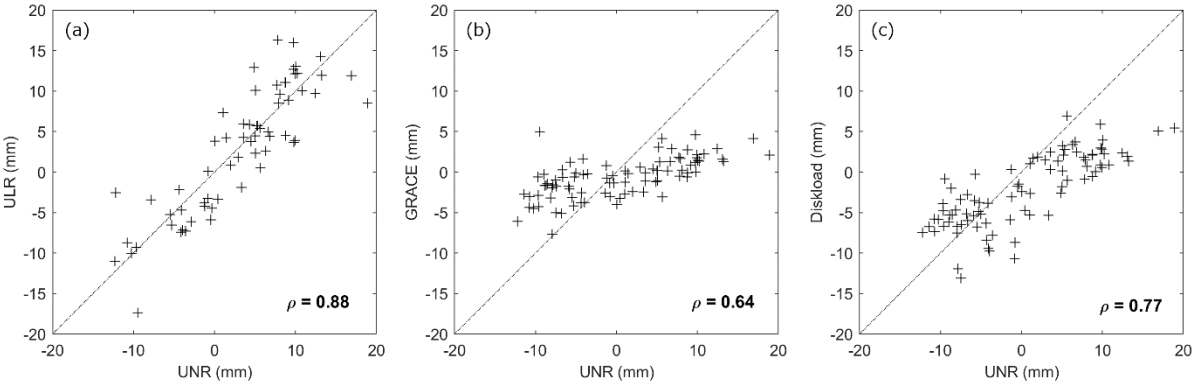

1078

1079 **Fig. 14.** Scatter plots of the vertical deformation between (a) GPS-UNR and GPS-ULR, (b) GPS-

1080 UNR and GRACE SHC, and (c) GPS-UNR and disk load model. The correlation coefficient (ρ)

1081 associated to each scatter plot is also given.

1082

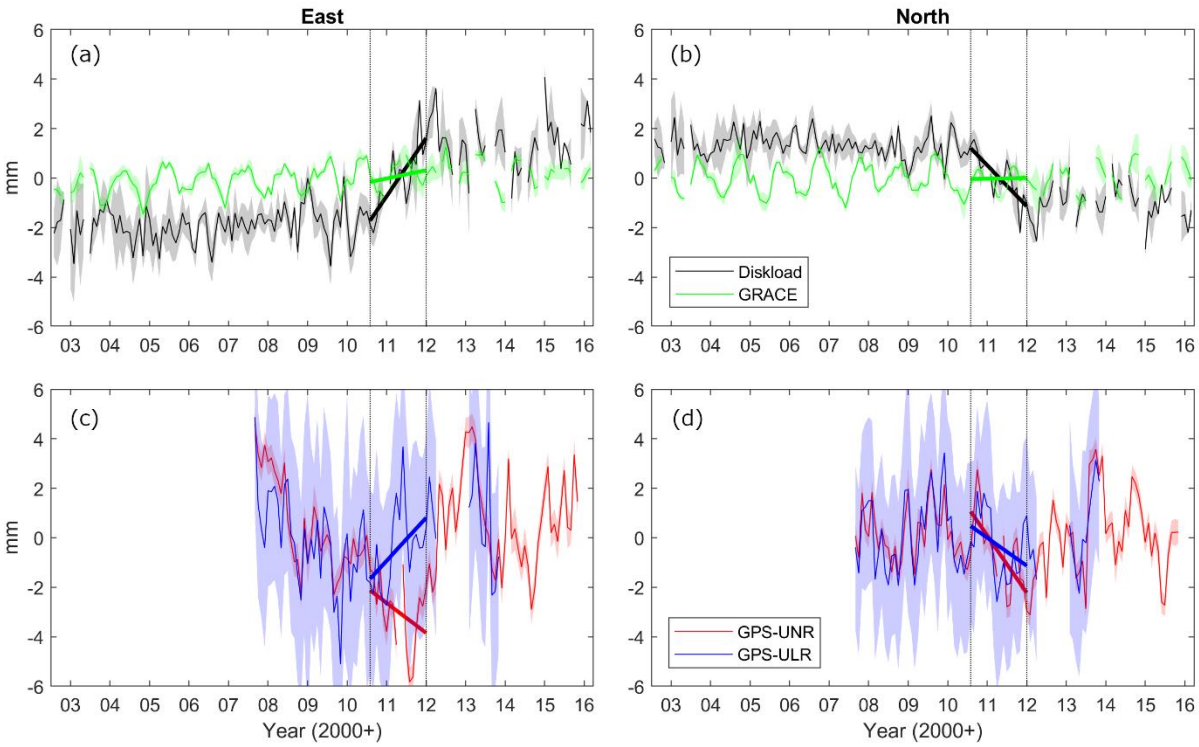

1083

1084 **Fig. 15.** The horizontal displacement ((a, c) East, (b, d) North) at BIN1 station computed using the
1085 disk load model, GRACE SHC data, and GPS observations (UNR, ULR). The vertical dotted lines
1086 between August 2010 and December 2011 denotes the impounding period. The thick solid lines are
1087 the estimated (fitted) trend during the impoundment, and the envelop represents the error of the
1088 displacement estimate.

1089

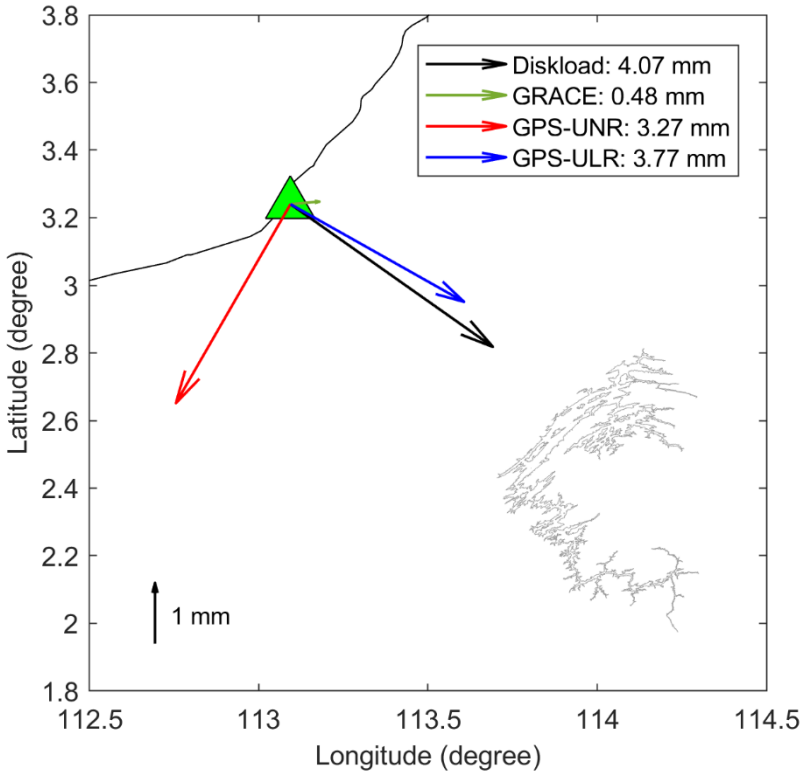

1090

1091 **Fig. 16.** The horizontal displacement ((a) East, (b) North) at BIN1 station computed using the disk
1092 load model, GRACE SHC data, and GPS observations (UNR, ULR). The vertical dotted lines
1093 between August 2010 and December 2011 denotes the impounding period. The thick solid lines are
1094 the estimated (fitted) trend during the impounding period.